Photoelectrocatalytic Reduction of CO_2 to Formate Using Immobilized Molecular Manganese Catalysts on Oxidized Porous Silicon

Young Hyun Hong,[1,2,5] Xiaofan Jia,[1,5] Eleanor Stewart-Jones,[1,5] Abhishek Kumar,[1] Justin C. Wedal,[1] Jose L. Alvarez-Hernandez,[1] Carrie L. Donley,[3] Albert Gang,[1] Noah J. Gibson,[1] Nilay Hazari,[1,6]* Madison Houck,[1] Sungho Jeon,[4] Jongbeom Kim,[4] Hyeongjun Koh,[4] James M. Mayer,[1,]* Brandon Q. Mercado,[1] Hannah S. Nedzbala,[1] Nicole Piekut,[1] Christine Quist,[1] Eric Stach,[4] and Yihui Zhang[4]

[1]Department of Chemistry, Yale University, P. O. Box 208107, New Haven, CT, 06520, USA. E-mail: nilay.hazari@yale.edu (lead contact[6]); james.mayer@yale.edu.

[2]Department of Chemistry and Center for Nano Materials, Sogang University, Seoul 04107, Republic of Korea.

[3]Department of Chemistry, University of North Carolina at Chapel Hill, Chapel Hill, NC, 27599, USA.

[4]Department of Materials Science and Engineering, University of Pennsylvania, Philadelphia, PA 19104, USA.

[5]These authors made equal contributions.

Summary

The selective reduction of CO_2 to formate using molecular catalysts immobilized on high surface area porous silicon is described. Manganese complexes of the form (^{R}bpy)Mn(CO)$_3$Br (bpy = 2,2'-bipyridine) were prepared with silatrane groups on the bpy ligand for attachment to oxide-coated porous silicon (SiO_x-porSi). SiO_x-porSi wafers were formed by heating hydrogen-terminated p-type porous silicon wafers under air and the manganese complexes were immobilized on SiO_x-porSi by heating at 80 °C. The resulting **Mn**@SiO_x-porSi photoelectrodes are photoelectrocatalysts for CO_2 reduction in acetonitrile containing 2.0 M triethylamine and 2.0 M isopropanol, yielding formate with high selectivity (>96%) and current density (~0.6 mA/cm^2), excellent reproducibility, and a photovoltage of 280 mV at -1.75 V (versus ferrocenium/ferrocene) under 1 sun illumination. The applied potential is close to the equilibrium potential for CO_2 reduction to formate. This work presents rare examples of immobilized molecular catalysts for CO_2 reduction to formate, and the first on semiconducting silicon.

Keywords

CO_2 reduction; immobilized catalysts; porous silicon; photoelectrocatalysis; formate production; base-metal catalysis.

Introduction

CO_2 is an attractive feedstock for the sustainable production of commodity chemicals and fuels because it is abundant, inexpensive, and non-toxic.[1-10] A variety of homogeneous[11-15] and heterogeneous[16-22] catalysts have been reported for photo-, photoelectro-, and electrochemical CO_2 reduction. Homogeneous catalysts often give high selectivity and are easy to tune but have limited stability. Heterogeneous catalysts are typically more stable and easier to separate but give lower selectivity and can be difficult to rationally modify. The immobilization of molecular catalysts on heterogeneous supports potentially provides the benefits of both homogeneous and heterogeneous catalysis as the molecular component can be tuned to give high selectivity, while the heterogeneous nature of the system improves practicality by facilitating separation.[23-26] Further, immobilized systems are especially valuable for photo-, photoelectro- or electrochemical processes where a conductive support can efficiently capture light and transport electrons to the attached catalyst.[27-33]

There are many examples of immobilized molecular catalysts on semiconducting supports that can photo-, photoelectro-, or electrochemically reduce CO_2 to CO.[34-43] In contrast, systems that can reduce *CO_2 to formate* (or formic acid) are rare.[44-54] The efficient generation of formate from CO_2 is potentially valuable because approximately one kiloton of formate is produced globally each year from fossil-based feedstocks.[55] Additionally, formic acid could be used for liquid organic chemical hydrogen storage or as a sustainable fuel in fuel cells.[56-58] The few examples of immobilized molecular catalysts for CO_2 reduction to formate typically use precious metal catalysts (often as polymer films) and are supported on metal oxides, such as TiO_2, metal or carbon nitrides, or graphene oxide (see S.XXII for table of previous systems).[45-54] In general, Faradaic efficiencies (FEs) are lower than 85% and most systems give relatively low current densities (below 0.4 mA/cm^2).

Semiconducting Si is an appealing support for molecular photo-, photoelectro-, or electrochemical catalysts because it is readily available, able to absorb light and separate charge, and its surface chemistry and electronic properties are well-understood due to its use in the electronics industry.[59] Nevertheless, there are relatively few examples of the immobilization of molecular catalysts on planar Si wafers, and these systems generally give poor catalytic performance.[60-66] This is partly because planar Si surfaces are highly reactive with oxygen, which complicates functionalization

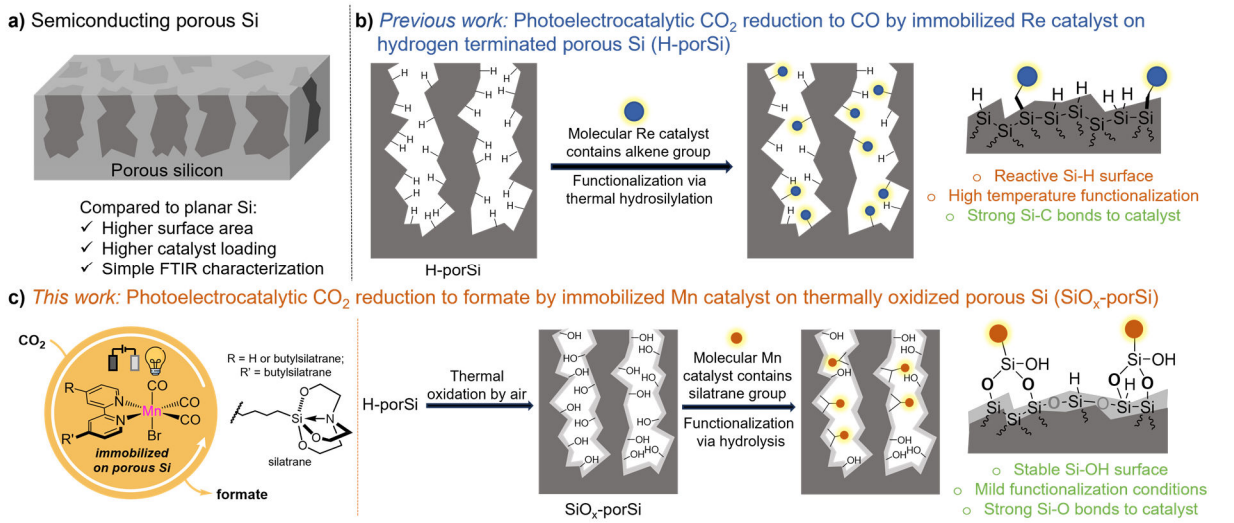

Figure 1: a) Comparison of porous Si with planar Si. **b)** Previous work immobilizing a molecular Re catalyst for photoelectrocatalytic CO_2 reduction to CO on hydrogen-terminated porous Si (H-porSi).[6i] **c)** This work immobilizing molecular Mn catalysts for photoelectrocatalytic CO_2 reduction to formate on thermally oxidized porous Si (SiO_x-porSi).

and reduces the stability of the hybrid material.[67-68] In addition, the low surface area of planar Si leads to modest amounts of catalyst on the surface, which can limit activity.

We recently described the first use of hydrogen-terminated p-type porous Si (H-porSi) as a photoabsorbing support for a molecular catalyst (Figure 1a).[43] The advantages of using porous Si compared to planar Si include high surface area,[69-70] unusual stability to oxygen at room temperature,[71] and facile characterization using transmission mode IR spectroscopy.[72] Using a modified Re compound immobilized on H-porSi we achieved high FEs for photoelectrocatalytic CO_2 reduction to CO with ~300 mV of photovoltage (Figure 1b).[43] Despite the impressive initial results achieved with porous Si,[43] several problems limit the ability of H-porSi to act as a general support for molecular catalysts: (i) To perform the hydrosilylation reaction for immobilizing the molecular catalyst on H-porSi it is necessary to have a pendant alkene group on the molecular catalyst and use high reaction temperatures (160 °C).[43,72-73] These requirements constrain the range of molecular catalysts that can be attached. (ii) H-porSi reacts with many common solvents, such as methanol, which reduces the choice of conditions for immobilization and catalysis.[74] (iii) Under the strongly reducing conditions required for CO_2 reduction, H-porSi is reactive and produces a significant amount of H_2 and can even generate a small amount of CO from CO_2.[75-76]

Previous studies have demonstrated that planar Si wafers are less reactive but maintain high conductivity if they are coated with a thin layer of SiO_2 or a metal oxide.[77] An oxide surface also

changes the strategies for covalent attachment of a molecular catalyst so that a greater range of functional groups, many of which form covalent bonds under mild conditions, can be utilized.[78-80] Thus, we hypothesized that by protecting H-porSi with a thin layer of SiO_2, we could produce a novel support with better properties for immobilizing molecular catalysts that could be an alternative for traditional semiconducting supports, such as TiO_2 and carbon nitride.[27-33]

Here, we describe photoabsorbing porous Si supports coated with a thin layer of thermally grown oxide (SiO_x-porSi); a new material for immobilizing molecular catalysts. We attach the first-row molecular catalysts (mono-silatrane-bpy)$Mn(CO)_3Br$ or (bis-silatrane-bpy)$Mn(CO)_3Br$ onto SiO_x-porSi using simple hydrolysis-type reactions that occur under mild conditions to generate porous Si based hybrid photoelectrodes (Figure 1c). The support and photoelectrodes were readily characterized using FTIR spectroscopy, which enabled a high level of reproducibility across samples. Our photocathodes are capable of photoelectrochemically reducing *CO_2 to formate* with excellent selectivity (>96%), current density (~0.6 mA/cm^2), and reproducibility, and a photovoltage of ~280 mV. Based on an open-circuit potential measurement of the proton activity under the catalytic conditions, the applied potential is approximately the equilibrium potential for CO_2 reduction to formate, with the additional potential provided by the photovoltage indicating that photoelectrocatalysis occurs at an overpotential of ~280 mV.

Our system represents one of the first immobilized molecular catalysts for CO_2 reduction to formate, and to our knowledge the first on any type of semiconducting Si. The high selectivity and current density make it one of the most effective immobilized systems for photoelectrocatalytic CO_2 reduction to formate (see Table S6 & Figure S97), with the added benefit that the catalyst is based on a first-row transition metal. We expect that this work will prompt further studies into the use of oxide or other coatings to stabilize and protect H-porSi. It will also facilitate the use of SiO_x-porSi as a potentially inexpensive and easy to use light absorbing semiconductor for immobilizing molecular catalysts for a range of transformations beyond CO_2 reduction.

Results and Discussion

Preparation of a Thermal Silicon Oxide Layer on Hydrogen-Terminated Porous Si (SiO_x-porSi)

One of the challenges associated with using H-porSi (and other types of hydrogen-terminated Si) as a support is that it is not possible to obtain a perfect monolayer of a catalyst via hydrosilylation for steric reasons.[81-82] As a consequence, Si-H bonds remain on the surface after catalyst

immobilization. Although the formation of a native oxide layer for freshly etched porous Si can be extremely slow under ambient conditions, the surface can oxidize when subjected to heat, which is required for hydrosilylation, or under the conditions used for CO_2 electroreduction.[43] The subsequent restructuring of the surface complicates analysis. In addition, the apparent production of H_2 from reactive Si-H sites[43] and the ability of some Si-H sites to reduce CO_2 stoichiometrically[75-76] introduces further complexity. We postulated that a solution would be to generate a dense, protective silicon oxide layer on H-porSi that does not change throughout functionalization and electrochemical experiments.[83]

H-porSi was prepared using a previously reported procedure in which low-doped p-type wafers (1-10 Ω cm^2) were assembled in a teflon cell, exposed to a 1:1 solution of HF:EtOH and 40 mA current was applied for five minutes (Figure 2a).[43] The H-porSi was characterized using FTIR spectroscopy, where three characteristic hydride stretches (νSi-H_x) are observed around ~2100 cm^{-1} (Figure S1) and scanning electron microscopy, which confirmed a porous morphology (Figures S2).

Relatively gentle heating of our H-porSi wafers to 190 °C was sufficient to create an oxide layer that does not cause physical damage to the porous structure and has surface Si-OH sites for catalyst attachment (Figure 2a). This is a much lower temperature than previous reports of formation of thermal oxides by heating porous Si (typically 700-1200 °C) in the presence of oxygen,[84-85] although the amount of heating required and damage to the porous structure depends on the exact type of porous Si. The formation of the oxide layer in these oxidized porous Si samples (SiO_x-porSi) was monitored by FTIR spectroscopy (Figure 2b). As soon as one hour after heating, the characteristic hydride stretches (νSi-H_x) around ~2100 cm^{-1} decrease as porous Si is oxidized. Stretches assigned to backbonded hydrides (νOSi-H) around ~2200 cm^{-1} and Si-oxygen bonds (νSi-O) around 1100 cm^{-1} appear. These changes are similar to those reported for oxidation of other porous Si samples.[86] The increase in the OH stretching band at ~3300 cm^{-1} is likely due to the generation of Si-OH bonds, but there could also be some physisorption of water molecules in the pores since the oxide is expected to be more hydrophilic than H-porSi. The predominance of hydrogen bonded OH groups at ~3300 cm^{-1} over isolated OH (ca. 3600 cm^{-1}) may also suggest the presence of water.

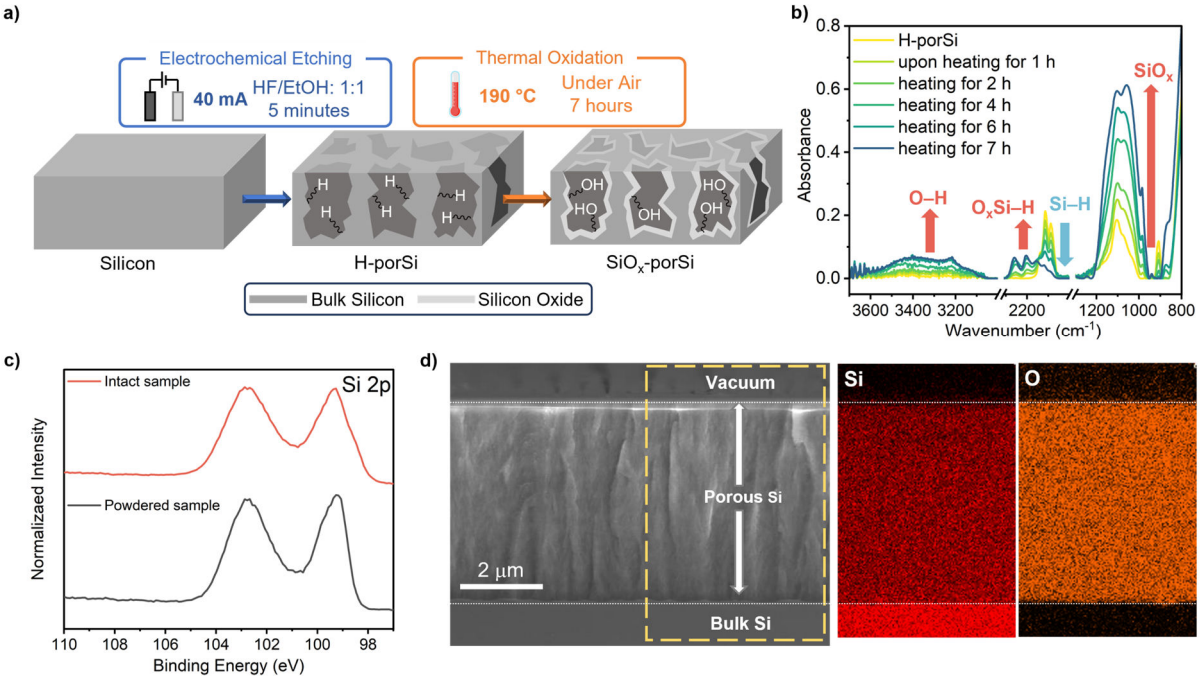

Figure 2: a) Schematic illustration of the preparation of SiO_x-porSi. Characterization of SiO_x-porSi: **b)** FTIR and **c)** Si 2p XPS spectra. The XPS spectra are of an intact sample, which is representative of the top 10-15 nm of the surface, and a powdered sample, which was obtained by scratching of the porous material and mixing and is representative of the entire pore. **d)** Cross-sectional SEM image and EDS mapping of Si and O in the area highlighted by the yellow rectangle.

While FTIR spectroscopy cannot be used to gauge the thickness or evenness of an oxide layer, the decrease of the initial Si-H_x stretch can be used to gauge the extent of oxidation.[72,87] In our case, after seven hours, the intensity of the Si-H_x stretches is reduced by approximately 80%, indicating the majority of Si atoms on the surface have been at least partially oxidized. We suggest that there is less than a monolayer of oxide present on the surface after seven hours of heating because Si-H_x stretches are still visible, indicating that the entire Si surface has not been oxidized. Based on our inability to detect any distinct oxide layer by microscopy we estimate the thickness of the oxide layer is less than 5 nm, but FTIR spectroscopy suggests the layer is not uniform. The presence of only a thin layer of oxide is likely optimal for electrocatalytic applications because electrons need to pass through this insulating SiO_2 layer. If the layer is too thick electrons may not reach the catalyst. It may be that the presence of surface hydrogen could also passivate some of the Si/SiO_2 interface states that can hinder photocatalysis.[88] Control experiments demonstrated that heating of H-porSi wafers at 190 °C for eighteen hours leads to a continued decrease in the Si-H_x features, suggesting the presence of a more uniform and thicker oxide layer (Figure S62). However, the electrocatalytic behavior is worse when a catalyst is immobilized on this material (*vide infra*).

Therefore, in this work we used SiO_x-porSi samples that had been heated for seven hours at 190 °C. A major advantage of the facile characterization of SiO_x-porSi using FTIR spectroscopy is that this technique can be readily used to ensure reproducibility across samples in the etching and oxidation steps by ensuring the absorbance of the νSi-H_x, νOSi-H, and νSi-O are comparable for the various SiO_x-porSi samples (Figure S3).

Samples of SiO_x-porSi were additionally characterized by XPS (Figures 2c, S4 & S5), BET (Figure S6), and cross-sectional SEM and EDS (Figure 2d). Since XPS typically only probes approximately the top 10 nm of a sample,[89] measurements were recorded on two types of samples, intact and powdered. Intact samples were unmodified SiO_x-porSi. The two characteristic Si 2p signals, at 99 and 103 eV, confirm the presence of both elemental Si and SiO_x, respectively, at the top of the pores (Figure 2c).[90-91] The powdered samples were created by scraping and grinding up the porous Si area and pressing the powder into indium metal. The Si 2p signal at 103 eV in the black trace in Figure 2c indicates that the oxide is found throughout the porous structure. BET analysis revealed that SiO_x-porSi is a high surface area material with an area of 70 m^2/g. Cross-sectional SEM confirms that the overall porous structure does not greatly change after oxidation (Figure 2d) and the sample of SiO_x-porSi shows roughly the same pore depth and structure as H-porSi. Further, EDS mapping shows a higher concentration of Si in the bulk Si than in the porous region and oxygen maps almost completely over the porous area. Taken together XPS and EDS confirm the presence of an oxide layer throughout the porous structure. Finally, as determined by FTIR spectroscopy, samples of SiO_x-porSi are stable when left in ambient conditions for at least seven days (Figures S7 & S8). Overall, SiO_x-porSi has many attractive qualities as a support because of its stability, reproducibility, facile fabrication, and easy characterization.

Synthesis and Characterization of Mn(I) Catalysts with Surface Attachment Groups

It was recently demonstrated that the Mn(I) complex (bpy)$Mn(CO)_3Br$ electrocatalytically reduces CO_2 to formate with a FE of approximately 60% in an acetonitrile (MeCN) solution containing 2.0 M isopropanol (^{i}PrOH) and 2.0 M triethylamine (NEt_3).[92] Given our interest in generating an immobilized system for CO_2 reduction to formate, we synthesized variants of (bpy)$Mn(CO)_3Br$ with functional groups on bpy that would enable covalent attachment SiO_x-porSi. To compare the performance of SiO_x-porSi to H-porSi as a support, we also prepared complexes with functional groups on bpy that would enable immobilization on H-porSi. The new complexes **1** and **2** contain

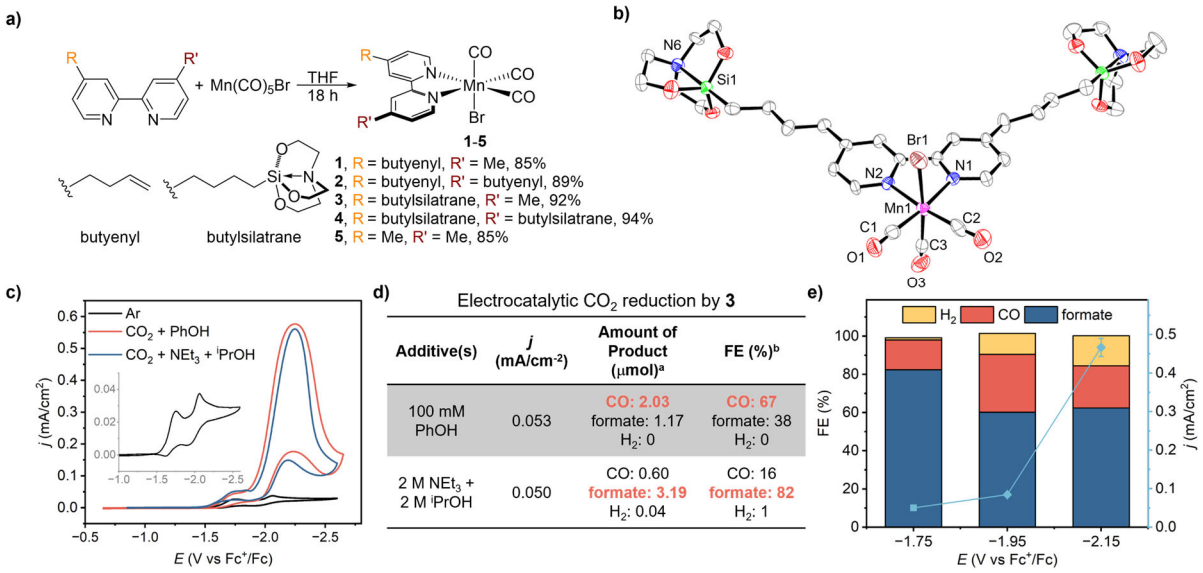

Figure 3: a) Synthesis of Mn complexes (**1-4**) with surface attachment groups and control compound **5**. **b)** Molecular structure of **4** with ellipsoids drawn at the 35% probability level. The small crystal size resulted in a low bond precision (see section S.XXI). **c)** Representative cyclic voltammograms of **3** in MeCN containing 0.25 M $^{n}Bu_4NPF_6$ under Ar (black), CO_2 and 100 mM PhOH (red), and CO_2, 2.0 M NEt_3 and 2.0 M $^{i}PrOH$ (blue). **d)** Performance of **3** in electrocatalytic CO_2 reduction in MeCN containing 0.25 M $^{n}Bu_4NPF_6$ in the presence of 100 mM PhOH or 2.0 M NEt_3 and 2.0 M $^{i}PrOH$ at -1.75 V. **e)** Comparison of product distribution with FE after forty minutes of CPE using a mixture of 1.0 mM **3**, 2.0 M NEt_3 and 2.0 M $^{i}PrOH$ at various potentials in a CO_2 saturated solution containing 0.25 M $^{n}Bu_4NPF_6$ in MeCN. Light blue line depicts current density obtained at 40 minutes in each experiment.

either one or two pendant alkenes, respectively, on the bpy ligand for immobilization through hydrosilylation to H-porSi. The new complexes **3** and **4** contain either one or two pendant silatrane groups, respectively, on the bpy ligand. The silatrane groups can undergo hydrolysis-type reactions with surface Si-OH groups to form strong Si-O bonds to the surface.[66] We selected the silatrane group because it is air and moisture stable and results in strong binding to metal oxide surfaces upon mild heating.[93-97] The literature compound (4,4'-Me_2bpy)$Mn(CO)_3Br$ (**5**, 4,4'-Me_2bpy = 4,4'-dimethyl-2,2'-bipyridine)[98] served as a control compound.

Complexes **1-5** were prepared in yields of 85-94% through the reaction of the substituted bpy ligands with $Mn(CO)_5Br$ in THF (Figure 3a & see section S.III). All complexes were fully characterized by ^{1}H and ^{13}C NMR, FTIR, and UV-Vis spectroscopies and HRMS (see section S.XX). Complex **4** was also characterized by single crystal X-ray diffraction analysis and has similar geometric parameters around Mn compared with related complexes without silatranes (Figure 3b & section S.XXI).[99] Cyclic voltammograms of complexes **1-5** were recorded in MeCN with $^{n}Bu_4NPF_6$ as the electrolyte under Ar (Figures 3c & S9). Two partially reversible redox events were observed at approximately -1.75 V and -2.2 V *vs.* ferrocenium/ferrocene (Fc^{+}/Fc). These are

assigned as reduction of the Mn center (Mn(I)/Mn(0)), followed by dimerization of Mn(0) and subsequent reduction of the dimer to formally Mn(-I), following literature reports of other (bpy)$Mn(CO)_3X$ (X = Cl or Br) complexes.[92,100-103] Cyclic voltammograms of **1-5** were recorded under 1 atm of CO_2 in the presence of either 100 mM phenol (PhOH) or with 2.0 M ^{i}PrOH and 2.0 M NEt_3. These conditions were selected because PhOH is a common acid for electrochemical CO_2 reduction using Mn complexes,[102] while results from Daasbjerg *et al* demonstrate that 2.0 M ^{i}PrOH and 2.0 M NEt_3 are optimal additives for producing formate.[92] Under both conditions the cyclic voltammograms display significant current enhancement at the potentials of both the first and second reduction waves (Figures 3c & S10-S13). The current enhancement at the second wave is more significant, but our results are consistent with electrocatalytic CO_2 reduction at both potentials. This is in agreement with the previously identified presence of low and high overpotential pathways for electrocatalytic CO_2 reduction by this class of catalysts.[92]

To determine the products from electrocatalytic CO_2 reduction using **1-5**, controlled potential electrolysis (CPE) was performed (Figures S14-S20). The headspace was analyzed using gas chromatography to detect CO and H_2, and aliquots from the reaction solution were analyzed by ion chromatography to detect formate. Figure 3d summarizes the results using **3** with different proton sources at potentials of -1.75 V. In the presence of PhOH, CO is the major product (FE = 67% after 2.5 hours), whereas in the presence of NEt_3 and ^{i}PrOH, formate is the major project (FE = 82% after 2.5 hours). This is consistent with previous results from Daajsberg *et al*.,[92] although in the case of **3** even higher FEs for formate are observed with NEt_3 and ^{i}PrOH compared to (bpy)$Mn(CO)_3Br$. As the applied potential was increased from -1.75 V to -2.15 V in the presence of NEt_3 and ^{i}PrOH, formate remains the major product although the FE decreases and more H_2 is produced (Figure 3e). There is an expected increase in current density at higher applied potentials. Similar results to **3** were observed for compounds **1**, **2**, **4**, and **5** in CPE experiments under CO_2 (Figures S14-S20). Overall, our combination of spectroscopic and electrochemical characterization, catalysis, and crystallographic data suggests that modifications made to the bpy ligand to enable immobilization do not significantly affect the reactivity of our series of Mn complexes, with **1-4** behaving analogously to **5**.

Catalyst Immobilization on Porous Si

We initially attempted to immobilize **1** and **2** through a hydrosilylation reaction with H-porSi using

the procedure we previously utilized for molecular Re complexes.[43,66] However, this strategy was not successful due to decomposition of **1** and **2** at the high temperatures required (160 °C). Attempts to perform the functionalization at lower temperatures (120 °C) did not lead to decomposition of **1** or **2** but no complex was immobilized as determined by FTIR spectroscopy, suggesting that high temperatures are required for hydrosilylation. An alternative strategy to facilitate hydrosilylation reactions is via sonication at room temperature,[104] but sonication of our H-porSi damaged the wafer. These experiments highlight some of the limitations associated with immobilizing reactive catalysts on H-porSi (see section S.V).

Complexes **3** and **4** were attached to SiO_x-porSi by heating a heterogeneous mixture containing an MeCN solution of the complex and a SiO_x-porSi wafer at 80 °C for eighteen hours (Figure 4a). The wafer was then rinsed with pentane and MeCN, soaked in 10 mL ethanol for an hour, and then rinsed again with pentane. To our knowledge this work represents the first occasion that molecular catalysts have been immobilized on oxidized porous Si and thus SiO_x-porSi is a new type of semiconducting support. The resulting hybrid materials, **3**@SiO_x-porSi and **4**@SiO_x-porSi, were characterized using a series of different techniques (Figures S21-S28). To quantify the amount of Mn attached to the surface, wafers of **3**@SiO_x-porSi and **4**@SiO_x-porSi were digested in 2.0 M KOH aqueous solution, then acidified with 70% nitric acid, and the extracts were analyzed by Inductively Coupled Plasma Mass Spectrometry (ICP-MS) (see SI for details, Table S1). Base was used because KOH dissolves the porous structure in approximately 10 minutes ensuring that all attached catalyst is digested. Samples from **3**@SiO_x-porSi and **4**@SiO_x-porSi with a geometric area of 1.2 cm^2 contained 810(80) nmol and 530(10) nmol, respectively, of Mn. The lower loading of **4** compared to **3** is likely related to the lower solubility of **4** as the solution is not completely homogeneous during immobilization.

FTIR spectroscopy was used to examine the attachment of **3** and **4** via their characteristic CO stretches and changes in the extent of oxidation of the SiO_x-porSi support (Figures 4b, S21 & S22). The FTIR spectra of **3**@SiO_x-porSi and **4**@SiO_x-porSi exhibited two prominent CO stretching bands between 1930 and 2030 cm^{-1} (Figure 4b). The frequency of the CO stretches is similar to those observed for powder samples of **3** and **4** suggesting that the complexes are still intact on the surface (Figures S90 & S91). Comparison of the FTIR spectra of **3**@SiO_x-porSi and **4**@SiO_x-porSi with that of SiO_x-porSi indicated that there is some further oxidation of the surface during

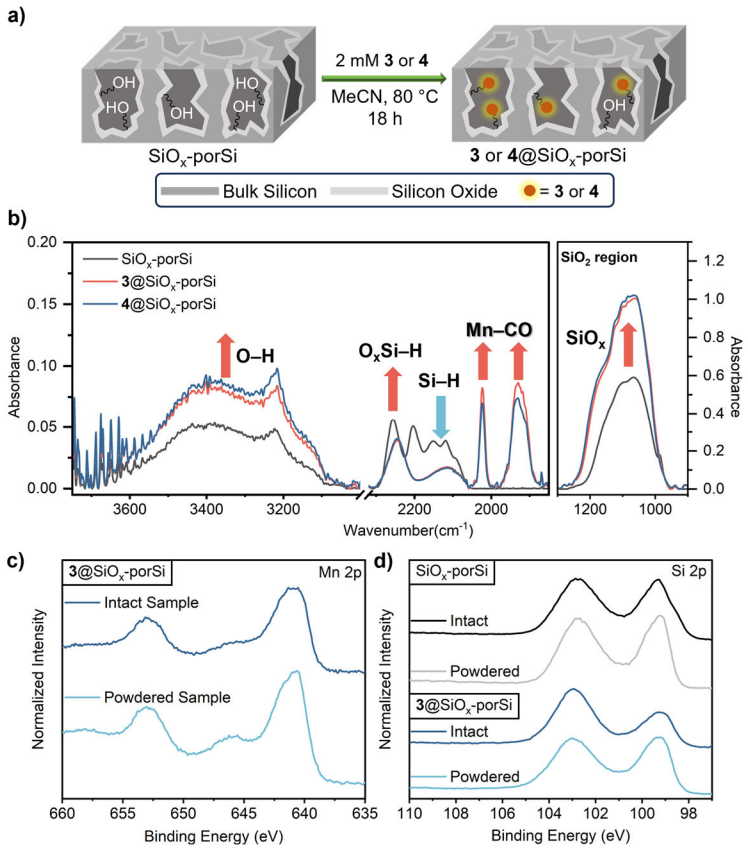

Figure 4: a) Schematic of the immobilization of **3** and **4** onto SiO_x-porSi. **b)** Characterization of **3**@SiO_x-porSi and **4**@SiO_x-porSi using FTIR spectroscopy. **c)** Mn 2p region XPS, and **d)** Si 2p region XPS spectra of **3**@SiO_x-porSi (see SI for data for **4**@SiO_x-porSi). The XPS spectra are of an intact sample, which is representative of the top 10–15 nm of the surface, and a powdered sample, which was obtained by scratching of the porous material and mixing and is representative of the entire pore.

silatrane attachment. This is not unexpected given that there were still some Si-H bonds on the surface of SiO_x-porSi, which likely react with trace O_2 and H_2O (in the MeCN) at 80 °C. The oxidation of surface Si-H bonds is supported by the 50% decrease in the intensity of the surface Si-H stretching bands at approximately 2100 cm^{-1}, along with an increase in the intensity of the v(Si-O) bands. Overall, the changes to the surface, as determined by FTIR spectroscopy, are significantly smaller upon catalyst attachment to SiO_x-porSi compared to H-porSi,[43] suggesting that it is a more stable support.

The XPS spectra of **3**@SiO_x-porSi and **4**@SiO_x-porSi were collected from both intact and powdered samples (Figures 4c, 4d, & S23-S26). Figure 4c shows the Mn 2p region of the XPS spectra of **3**@SiO_x-porSi, while the related data for **4**@SiO_x-porSi is in Figure S26. For **3**@SiO_x-porSi and **4**@SiO_x-porSi the Mn 2p doublet was observed for intact and powdered samples providing evidence for the presence of Mn both on the surface and in the pores. The major Mn

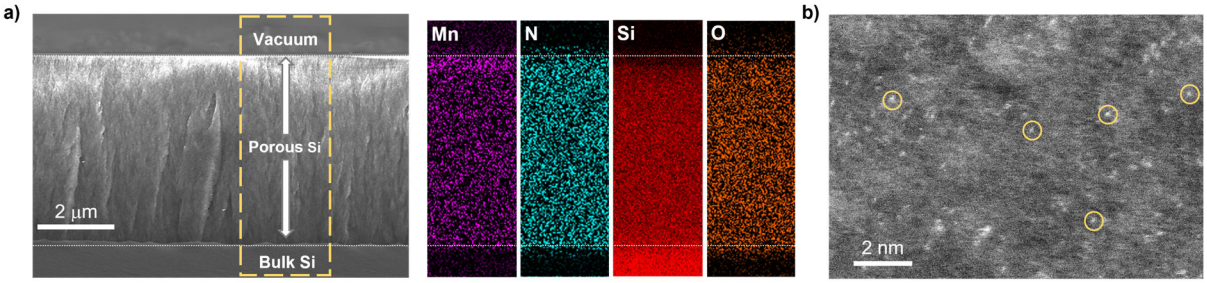

Figure 5: Characterization of **3**@SiO_x-porSi using microscopy. **a)** Cross-sectional SEM image and EDS mapping in the area highlighted by the yellow rectangle. **b)** AC-STEM high-angle annular dark field (HAADF) image of the porous Si region. Selected bright spots are highlighted in yellow circles.

peaks appear at ~654 eV and ~641 eV, consistent with Mn in the +1 oxidation state and the presence of an immobilized version of **3** or **4**.[105] Additionally, the Mn 2p spectra exhibit weaker satellite peaks at ~646 and ~658 eV. These same satellite peaks are observed in powered samples of molecular **3** and **4**, again suggesting that the complexes are intact on the surface. A comparison of the Si 2p region of the XPS spectra of powdered **3**@SiO_x-porSi (which examines the bulk sample) with unfunctionalized SiO_x-porSi indicates the ratio of silicon oxide (~103 eV) to elemental Si (~99 eV) remained relatively unchanged, suggesting no significant change to the bulk. However, a slight increase in the ratio of silicon oxide to Si was observed in the intact samples of **3**@SiO_x-porSi suggesting there was some surface oxidation during immobilization in agreement with results from FTIR spectroscopy and our previous observations for immobilization of a Re catalyst on H-porSi through hydrosilylation.[43]

Cross-sectional SEM showed that the internal pore structures of **3**@SiO_x-porSi and **4**@SiO_x-porSi were similar to that of SiO_x-porSi, highlighting that the catalyst immobilization procedure did not significantly impact the wafer structure (Figures 5a & S27). EDS elemental mapping spectra were used to elucidate the elementary composition inside the pores of **3**@SiO_x-porSi and **4**@SiO_x-porSi (Figures 5a & S27). These spectra show that Mn and N are both present throughout the porous section of the material, consistent with the intact catalyst being present in the pores. To further test for the presence of **3** in the pores of **3**@SiO_x-porSi, a cross-section of **3**@SiO_x-porSi was observed at high magnification using aberration-corrected scanning transmission electron microscopy (STEM). To meet the electron transparency requirement for STEM observation, we made a thin layer (lamella) of the sample using a focused ion beam (FIB) lift-out technique (see SI for more information). A high-magnification high-angle annular dark field (HAADF) image from the porous Si area is shown in Figure 5b. HAADF images amplify imaging intensity according to ~Z^2.[106] The image contains many bright spots, consistent with their assignment as individual Mn atoms.

Further, when EDS and electron energy loss spectroscopy (EELS) were performed on a sample region containing the bright spots, the Mn K and L edges are clearly observed in the EDS and a peak at around 644 eV, corresponding to Mn, is detected by EELS (Figure S28).[107]

To gain evidence for covalent attachment of the complexes, a solution of **3** in MeCN was drop-cast onto a SiO_x-porSi wafer, which presumably resulted in physisorption of **3** (Figure S31). The CO region of the surface FTIR spectrum of this sample showed peaks at 2026 and 1938 cm^{-1}. However, when the SiO_x-porSi wafer containing the drop-cast sample was washed with MeCN, no signals associated with the CO stretches remain in the IR spectrum, suggesting that our procedure of soaking in MeCN removes any complexes physisorbed to the surface. Moreover, soaking a SiO_x-porSi wafer in an MeCN solution of **5** under N_2 at 80 °C for eighteen hours and subsequently washing the wafer with pentane and ethanol (the same functionalization procedure used for **3** and **4**) resulted in no CO stretches being observed by FTIR spectroscopy (Figure S32). This was expected since **5** lacks a functional group for covalent attachment to the surface. Overall, our characterizing data shows that **3** and **4** have been successfully immobilized on SiO_x-porSi and are likely intact and present in the pores of the material. Covalent attachment of the complexes is supported by washing experiments and the electrochemical results described in the next section.

*Photoelectrochemical CO_2 Reduction Using **3**@SiO_x-porSi and **4**@SiO_x-porSi*

Cyclic voltammograms were obtained for **3**@SiO_x-porSi and **4**@SiO_x-porSi in contact with an electrolyte solution, 0.25 M $^nBu_4NPF_6$ in MeCN, with one sun illumination under Ar or CO_2, in the absence of any added proton source. All the cyclic voltammograms (and the linear sweep voltammogram for **3**@SiO_x-porSi) are quite similar, with a gradual increase in current density observed starting at approximately -1.2 V (Figures 6a, S35-S38). We attribute the lack of well-defined signals for the immobilized catalyst to the complexities associated with using porous Si as an electrode, which have been described previously.[43] A notable feature of the cyclic voltammograms of **3**@SiO_x-porSi under Ar and CO_2 with one sun illumination is that the initial scan is similar to subsequent scans. This stands in contrast to our previous studies using catalysts immobilized on H-porSi, where the initial cyclic voltammograms were dominated by electrochemical reactions that occur at the surface.[43] The absence of an initial surface response from SiO_x-porSi suggests a low level of electroactive surface states and indicates that it is a better-behaved system for immobilizing molecular electrocatalysts, compared to H-porSi.

When cyclic voltammograms of **3**@SiO_x-porSi and **4**@SiO_x-porSi were recorded with one sun illumination under a CO_2 atmosphere in the presence of 2.0 M NEt_3 and 2.0 M ^{i}PrOH, significant photoelectrocatalytic current density is observed with an onset potential[108] of approximately -1.32 V (Figures 6a, 6b, S36 & S37). The current remains constant in five consecutive scans, suggesting that a stable photoelectrocatalytic process is occurring (Figure 6b). Similarly, when cyclic voltammograms of **3**@SiO_x-porSi and **4**@SiO_x-porSi were recorded with one sun illumination under a CO_2 atmosphere in the presence of 100 mM PhOH, current associated with a photoelectrocatalytic event was observed (Figure S38). Control experiments with a photoelectrode that had been subjected to the silatrane immobilization conditions but without the Mn catalyst (denoted as SiO_x-porSi$^{\Delta}$) did not show a significant amount of current under our standard conditions (one sun illumination, CO_2 atmosphere, 2.0 M NEt_3, and 2.0 M ^{i}PrOH; Figures 6b & S39). A small amount of current is generated when SiO_x-porSi$^{\Delta}$ is reduced under a CO_2 atmosphere with 100 mM PhOH in the presence of 1 sun illumination, but this is far less than for systems containing Mn (Figure S39). These results show that the presence of Mn is required to generate significant current density during photoelectrocatalysis.

We used CPE at -1.75 V to examine the product distribution from photoelectrocatalytic reduction of CO_2 using **3**@SiO_x-porSi under our standard conditions (Figures 7a & 7b). Seven hours of CPE with **3**@SiO_x-porSi formed 25.5 μmol of formate with ~7 C of charge passed (Figures 7a). This corresponds to a FE for formate of 71%, with only a small amount of H_2 generated and almost no CO. No liquid products, such as methanol, were detected using NMR spectroscopy after seven hours of CPE. Earlier in the electrolysis, after forty minutes, the FE for formate was a remarkable 96%, with almost no detectable H_2 or CO generated.

The geometric current density in the CPE experiments decreased by 33% from its maximum at 0.6 mA/cm^2 after forty minutes to 0.4 mA/cm^2 after seven hours.[109] The geometric current density observed in CPE after forty minutes is similar to the current density observed in cyclic voltammetry at -1.75 V. This further indicates a relatively stable catalytic system. Based on the geometric current density from CPE after forty minutes and the amount of Mn on the surface (from ICP-MS), the maximum TOF to formate at -1.75 V is 11 h^{-1}.

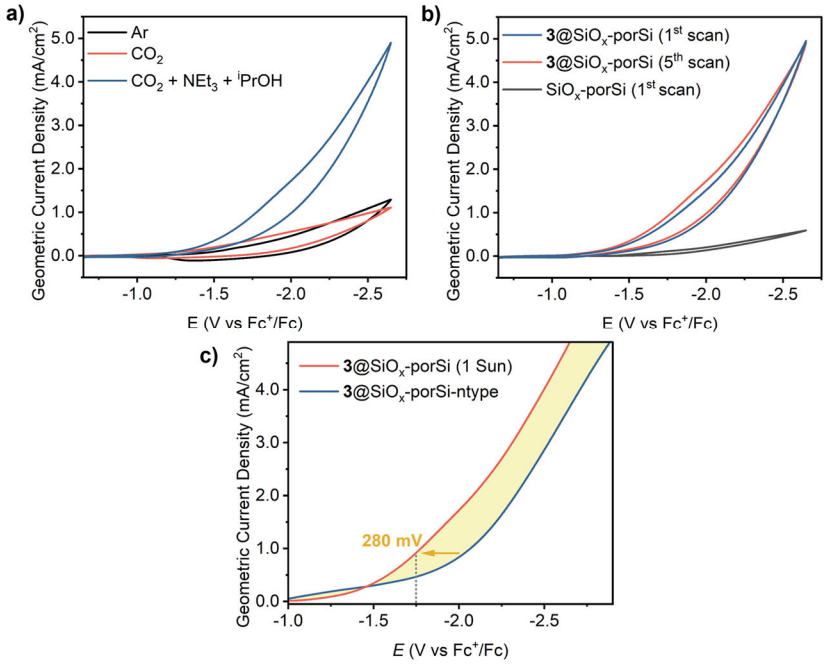

Figure 6: Electrochemistry of **3**@SiO_x-porSi as the working electrode in CO_2 saturated solutions (except as noted), all containing 0.25 M $^nBu_4NPF_6$ in MeCN with 2.0 M NEt_3 and 2.0 M ^{i}PrOH (our standard conditions). **a)** Cyclic voltammograms of **3**@SiO_x-porSi under Ar (black), CO_2 (red), and CO_2 with 2.0 M NEt_3 and 2.0 M ^{i}PrOH (blue) under 1 sun illumination. **b)** 1st (blue) and 5th scan (red) of **3**@SiO_x-porSi and 1st (black) scan of SiO_x-porSi$^\Delta$ under 1 sun illumination. **c)** Linear sweep voltammogram of **3**@SiO_x-porSi (red, under 1 sun illumination) and **3**@SiO_x-porSi-*n*type (blue, recorded in the dark).

The product distribution for CPE experiments after forty minutes using **3**@SiO_x-porSi under our standard conditions showed a strong dependence on the applied potential, over the range from -1.55 V to -2.15 V (Figure 7c & S45-48). The optimal FE was observed at -1.75 V, 96% as stated above. At a less forcing potential, -1.55 V, only small amounts of formate (1.22 μmol), H_2 (1.10 μmol), and CO (0.83 μmol) were made, each with low FE. At potentials more negative than the optimal, -1.95 V and -2.15 V, the geometric current density was higher (light blue line in Figure 7c) but the FE for formate decreased to 81% and 60%. The TOF to formate was relatively independent of applied potential, from 11 h^{-1} at -1.75 V to 12 h^{-1} at -2.15 V.

As a control experiment, we performed CPE evaluating the photoelectrocatalytic activity of a SiO_x-porSi$^\Delta$ electrode, which does not contain an attached catalyst. Under our standard conditions very little charge was passed, ~0.5 C after four hours, and the predominant product was H_2 (1.0 μmol) with almost no detectable CO and formate (Figure S55). This is consistent with the cyclic voltammetry results described above. Thus, the immobilization of **3** is crucial for generating significant quantities of formate, and SiO_x-porSi$^\Delta$ by itself is not efficient for CO_2 reduction.

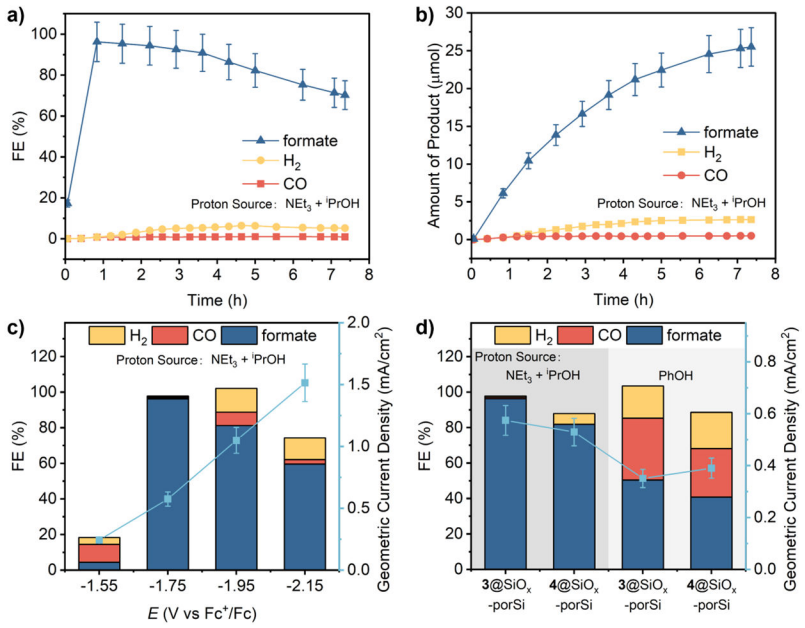

Figure 7: Photoelectrocatalytic CO_2 reduction using **3**@SiO_x-porSi as the working electrode in a CO_2 saturated solution containing 0.25 M $^nBu_4NPF_6$ in MeCN in the presence of 2.0 M NEt_3 and 2.0 M ^{i}PrOH. **a)** Cumulative FE versus time and **b)** cumulative amounts of formate, CO and H_2 in a CPE experiment with 2.0 M NEt_3 and 2.0 M ^{i}PrOH at -1.75 V versus Fc^+/Fc using **3**@SiO_x-porSi under 1 sun illumination. **c)** Comparison of product distribution for CO_2 reduction with FE after forty minutes of CPE at various potentials. Blue line depicts geometric current density measured at forty minutes. **d)** Comparison of product distribution for CO_2 reduction with FE after forty minutes of CPE using **3**@SiO_x-porSi and **4**@SiO_x-porSi at -1.75 V in the presence of 2.0 M NEt_3 and 2.0 M ^{i}PrOH or 100 mM PhOH in MeCN containing 0.25 M $^nBu_4NPF_6$ with 1 sun illumination. Blue line depicts geometric current density measured at forty minutes.

A photovoltage for electrocatalysis of approximately 280 mV was obtained by comparing the current density produced by **3**@SiO_x-porSi versus a photoelectrode containing **3** immobilized on a degenerately doped n-type porous Si wafer at a potential of -1.75 V using cyclic voltammetry (Figure 6c; see section S.X for experimental details). The 280 mV photovoltage is consistent with the many reported photovoltages using p-type Si photoelectrodes (0.2 to 0.6 V).[43,104,110-114]

Another important parameter for (photo)electrochemical CO_2 reduction is the overpotential, the difference between the applied potential and the equilibrium potential under the catalytic conditions. The reduction of CO_2 to formate is a $2e^-$, $1H^+$ reaction (Eq 1), so the equilibrium potential depends on both the applied potential and the solution proton activity, a_{H^+}.

$$CO_2 + 2e^- + H^+ \rightarrow HCOO^- \quad \text{(Eq 1)}$$

The solution a_{H^+} is challenging to estimate for the catalytic conditions due to uncertainty about the species present in CO_2-saturated MeCN with 2M Et_3N, 2M ^{i}PrOH, and 0.25 M $^nBu_4NPF_6$. This mixed solvent system likely contains species such as $^iPrOCO_2^-$.[92] We therefore directly measured the a_{H^+} under these conditions, using a previously reported method.[115-116] As described in section

S.XII, open circuit potentials were measured *vs.* $Fc^{+/0}$ for a hydroquinone/quinone couple in the presence of six buffers with known pK_a values, to generate a calibration line. The potential for the same couple under our catalytic conditions ($MeCN/CO_2/Et_3N/^iPrOH/^nBu_4NPF_6$) showed that the a_{H^+} was equivalent to that of a buffer with a pK_a of 21.9, so $a_{H^+} = 10^{-21.9}$ (Figures S57-S58 & Table S2). An equivalent experiment using 100 mM PhOH in ^{i}PrOH gave $a_{H^+} = 10^{-18.2}$. These are surprisingly high and similar acidities, given the pK_a of ^{i}PrOH, and suggest that the a_{H^+} in these solutions was determined by a carbonate-derived buffer.

Using the measured $a_{H^+} = 10^{-21.9}$ for our standard conditions, the equilibrium potential for Eq 1 was estimated to be –1.7 ± 0.1 V *vs.* $Fc^{+/0}$ (see section S.XII). This is within the experimental uncertainty we used for CPE experiments, -1.75 V, and the cyclic voltammetry and variable potential CPE experiments showed that catalysis was observed at potentials less negative than -1.75 V. Thus, we conclude that the photoelectrochemical reduction of CO_2 to formate by **3**@SiO_x-porSi can occur at roughly the equilibrium potential. The ~280 mV photovoltage from the Si absorber compensates for the overpotential of the Mn molecular catalyst.

To evaluate whether the SiO_x-porSi material (and not **3**) was responsible for absorbing light in our photoelectrocatalytic system, we performed a CPE experiment with **3**@SiO_x-porSi under our standard conditions using only red-light excitation, between 600-700 nm (Figure S59). At this wavelength **3** does not absorb (Figure S93). After 5 hours ~20 μmols of formate were produced, which is almost the same as under the standard conditions, and consistent with a small decrease in the geometric current density. The FE for formate was ~95%, with almost no detectable H_2 or CO generated. Thus, photoelectrocatalytic reduction of CO_2 using **3**@SiO_x-porSi results from the light absorption properties of Si, which facilitates charge separation, and multielectron catalysis by the attached Mn complex. An experiment with variable irradiation from the solar simulator showed that the CPE current density for CO_2 reduction using **3**@SiO_x-porSi was dependent on the light intensity, from 1 to 0.01 sun (Figure S60). After irradiation and then leaving **3**@SiO_x-porSi in the dark under our standard conditions, resubjecting the sample to one sun illumination returned the CPE to the original current. LSV scans with **3**@SiO_x-porSi also showed changes in current with variation in light intensity (Figure S40).

The length of time that H-porSi was oxidized also influences catalytic performance. A sample which was oxidized for eighteen hours before the immobilization of **3** and contains a thicker oxide

layer (IR spectroscopy indicated that no Si-H bonds were present on the surface) generated less formate with a lower FE (~60% after 45 minutes) than under the standard conditions (Figures S62 & S63). A significant amount of H_2 (~25% FE after 45 minutes) was also formed. This result suggests that the ideal thickness of the SiO_x coating for the photoelectrocatalysis performed in this work is less than a monolayer. This stands in contrast to the ideal, protective SiO_2 layer for a transistor, which is uniform, and does not contain a range of bonding environments on the surface.[117] The fact that the surface of our SiO_x-porSi is relatively heterogeneous, with Si-OH, OSi-H, Si-H, and O-Si bonds all present after oxidation (*vide supra*), indicating that we have not fully oxidized the surface, is likely important for allowing electrons to reach the immobilized catalyst.

To complement our experiments with **3**@SiO_x-porSi, we determined the product distribution from photoelectrocatalytic CO_2 reduction using **4**@SiO_x-porSi through a CPE experiment at -1.75 V under our standard conditions (Figures 7c & S49). After forty minutes the FE for formate was 82%, and unlike for **3**@SiO_x-porSi a measurable amount of H_2 was generated (FE_{H2} = 6%). The maximum TOF to formate of **4**@SiO_x-porSi at -1.75 V after forty minutes is 13 h^{-1}, slightly higher than for **3**@SiO_x-porSi. Other trends for **4**@SiO_x-porSi are the same as for **3**@SiO_x-porSi. For example, the catalytic activity of **4**@SiO_x-porSi decreased by a factor of 20% over seven hours at -1.75 V (compared to 25% for **3**@SiO_x-porSi) and the current density increased as the applied potential in photoelectrocatalysis is increased from -1.75 V to -2.15 V (Figures S50-S52). Notably, although the FE for formate decreases with increasing applied potential for **4**@SiO_x-porSi, the decrease is smaller than for **3**@SiO_x-porSi (from 81% to 72% for **4**@SiO_x-porSi *vs.* from 96% to 60% for **3**@SiO_x-porSi). The maximum TOF to formate for **4**@SiO_x-porSi was achieved at -2.15 V and is 23 h^{-1}. The reasons for the slightly different selectivity of **3** and **4** when they are immobilized are unclear, especially given their similar selectivity in solution. However, the different loadings of **3** and **4** when they are immobilized leads to an imperfect comparison and may itself be the cause of the variation in selectivity.

The performance of **3**@SiO_x-porSi and **4**@SiO_x-porSi for photoelectrochemical CO_2 reduction to formate are among the best immobilized systems in terms of *selectivity*, *current density per geometric area*, *TOF*, and *stability* (see Figure S97). Most previously reported systems give FEs to formate which are lower than 85% and display little activity after seven hours.[45-54] Another

attractive feature of **3**@SiO_X-porSi is that the catalytic results are reproducible. Three separate trials gave very similar kinetics for product formation, FEs, and current densities (Figure S61). The high reproducibility is likely in part due to our ability to characterize the initial H-porSi wafer, the oxidized SiO_x-porSi wafer, and the surface coverage of **3** using transmission FTIR spectroscopy. This degree of control is rare in the immobilization of molecular catalysts on solid supports.

The selectivity of photoelectrocatalytic CO_2 reduction achieved with **3**@SiO_x-porSi and **4**@SiO_x-porSi is higher than for electrochemical reduction of CO_2 in solution by **3** and **4** under our standard conditions (without illumination in solution). For example, the FE to formate is 96% with **3**@SiO_x-porSi compared with 82% for **3** in solution (after 40 minutes, at -1.75 V, standard conditions, Figures 3e & 7c). The higher formate selectivity with **3**@SiO_x-porSi was more dramatic when 100 mM PhOH was the proton source. In solution both **3** and **4** generate formate as only the minor product (FEs for formate, 38 and 36% respectively), while immobilized, **3**@SiO_x-porSi and **4**@SiO_x-porSi at -1.75 V with 1 sun illumination generate formate as the major product, with FEs of 54 and 41%, respectively (Figures S53 & S54). In solution, CO is the major product for both **3** and **4** (FEs for CO are 67 and 61%, respectively; Figure S18), while in the immobilized systems CO is the minor product (the FEs for CO are 37 and 27%, respectively).

At this stage it is unclear why the selectivity to formate increases when the catalyst is immobilized, one possible explanation is that the porous structure leads to variation in proton activity in different places along the pores, which could result in preferential formate production. Future work will explore why immobilization on the porous structure leads to different selectivity and explore diffusion rates in the porous material. Nevertheless, the higher selectivity to formate observed in our immobilized system is notable.

*Catalyst Leaching and Characterization of **3**@SiO_x-porSi and **4**@SiO_x-porSi after CPE*

A common problem in using molecular catalysts that are immobilized on solid supports is catalyst leaching into solution, and in some cases the leached material is responsible for catalysis.[118] We showed independently that leaching of **3** and **4** into solution is unlikely to be responsible for any photochemical CO_2 reduction by demonstrating that they do not produce formate from CO_2 in solution under the same reaction conditions used for **3**@SiO_x-porSi and **4**@SiO_x-porSi without an applied potential (see section S.XVI). Further, analysis of the CO region of the FTIR spectroscopy

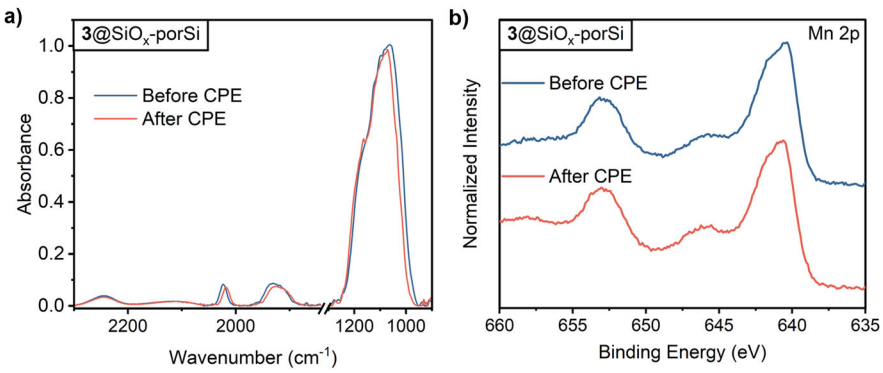

Figure 8: a) Overlay of FTIR spectra, and **b)** Mn 2p region XPS of **3**@SiO_x-porSi before (black) and after (red) CPE experiment with 2.0 M NEt_3 and 2.0 M $^{i}PrOH$ at -1.75 V versus Fc^{+}/Fc.

of **3**@SiO_x-porSi and **4**@SiO_x-porSi before and after CPE under our standard conditions for seven hours showed that ~86% and ~91%, of the Mn was still present after CPE in the form of complexes of the type (^{R}bpy)$Mn(CO)_3X$ (X = solvent or atom from support; see Figures 8a & S65-S73). XPS further supported the presence of Mn complexes on the porous Si after CPE (Figure 8b). ICP-MS quantitation with **3**@SiO_x-porSi after CPE also showed that 88% of the Mn was still present on the SiO_x-porSi photocathode, with only 12% of the Mn in the solution (Table S4). Cross-sectional SEM and EDS elemental mapping showed similar internal pore structures and elemental distributions for **3**@SiO_x-porSi and **4**@SiO_x-porSi before and after CPE (Figures S72 & S73). These results suggest that the immobilization of molecular catalysts on SiO_x-porSi results in a relatively small amount of catalyst leaching or surface restructuring.

The small amount of catalyst leaching (~10%) of **3** or **4** from SiO_x-porSi is contrasted by the more significant decrease in geometric current density during photoelectrolysis (~33% over 7 hours for **3**@SiO_x-porSi). This is coupled with a decrease in FE efficiency to formate and a decline in the overall FE from close to 100% to 75% over 7 hours. Control experiments indicate that formate is stable under the reaction conditions and that it is not trapped in the pores of the SiO_x-porSi support (see S.XIX). Hence, an unknown process is leading to a loss of catalytic performance by consuming electrons to generate a product that is not detected. Further, there is larger than expected current drop based on the amount of intact Mn complex on the surface, perhaps implying that a catalytically inert Mn species with a similar IR spectrum to immobilized **3** or **4** is formed. Nevertheless, the stability of **3**@SiO_x-porSi and **4**@SiO_x-porSi is higher than other immobilized molecular catalysts for formate production.[45-54] Additionally, the stability of **3**@SiO_x-porSi and **4**@SiO_x-porSi, contrasts with the instability of **3**, **4**, and related compounds[119-121] under

illumination in solution. This added stability was an unexpected benefit of immobilization in this system.

The differences in catalytic performance between immobilized **3** and **4**, in terms of initial FE to formate (*vide supra*) and stability, indicates that further tuning of the molecular catalyst and attachment group may lead to improved systems. There do appear to be some advantages in terms of the stability of the catalytic systems associated with attaching through a bis silatrane system and creating more soluble bis silatrane systems may be advantageous as this will enable higher catalyst loadings on SiO_x-porSi with bis silatrane complexes.

Conclusions

This work describes the first use of SiO_x-porSi in photoelectrocatalysis. SiO_x-porSi is a novel light-absorbing semiconducting material with a thin layer of thermally grown SiO_2 that both protects the underlying Si and serves as a support for a molecular catalyst. The results we report here demonstrate that SiO_x-porSi is an excellent support because: (i) it is stable under ambient conditions; (ii) it can readily be characterized by FTIR spectroscopy, which ensures reproducibility between samples; (iii) molecular catalysts can be attached to it under mild reaction conditions; (iv) it is relatively stable under the reducing conditions used in CO_2 reduction and consequently the surface does not produce large amounts of H_2 in contrast to H-porSi.[43] The superior properties of SiO_x-porSi as a support were demonstrated by synthesizing and immobilizing two molecular Mn complexes, **3** and **4**, containing bpy ligands modified with silatrane groups, which form strong Si-O bonds with the surface. FTIR spectroscopy, XPS, SEM, and STEM confirmed that the Mn complexes were located throughout the porous structure.

The photoelectrodes, **3**@SiO_x-porSi and **4**@SiO_x-porSi, were highly selective for the photoelectrocatalytic reduction of CO_2 to formate. The highest FE for formate of 96% was achieved with **3**@SiO_x-porSi using a CO_2-saturated MeCN solution containing NEt_3 and ^{i}PrOH at an applied potential of -1.75 V under 1 sun illumination. Apart from this unprecedented FE for an immobilized system, the hybrid photoelectrodes also display excellent current density (~0.6 mA/cm^2), stability (~7 hours), and reproducibility compared to previous examples in the literature.[45-54] Our current hypothesis is that the mechanism for CO_2 reduction using **3** or **4** immobilized on SiO_x-porSi involves the same elementary steps and intermediates as CO_2 reduction using **3** or **4** in solution,[92] but further work is required to validate this proposal. Two other notable

features of **3**@SiO_x-porSi and **4**@SiO_x-porSi are that: (i) once immobilized, the Mn complexes do not appear to decompose upon exposure to light, as they do in solution, and (ii) the hybrid photoelectrodes display higher selectivity to formate than the molecular catalysts in solution. In the future, we intend to study how the pore structure influences catalyst selectively and stability and to map diffusion gradients in the pores.

Overall, our strategy of using a thin layer of SiO_2 to protect porous Si is likely to be broadly useful for various coatings and molecular catalysts and a range of photoelectrochemical reactions. This is because there are several methods available for forming oxides on porous Si, numerous easily installed functional groups for attachment to SiO_x and related metal oxides, and the hydrolytic attachments are readily accomplished under mild conditions. The value of the SiO_x-porSi and related materials was illustrated here by the robustness and high FE of **3**@SiO_x-porSi for the photoelectrochemical reduction of CO_2 to formate.

Experimental Procedures

Resource availability

Lead contact

Further information and requests for resources should be directed to and will be fulfilled by the lead contact, Nilay Hazari (nilay.hazari@yale.edu).

Materials availability

Detailed information about the preparation and characterization of new compounds is provides in the supplemental information.

Data and code availability

Crystallographic data have been deposited in the Cambridge Crystallographic Data Center (CCDC) with the following accession number: **4** (2368434). The data can be obtained free of charge from the CCDC at https://www.ccdc.cam.ac.uk/structures/.

Generic protocol for Controlled Potential Electrolysis (CPE) with hybrid photoelectrodes

CPE experiments were conducted in the two-compartment H-cell as the cyclic voltammetry experiments. The working compartment consisted of 250 mM $^nBu_4NPF_6$ and 2.0 M NEt_3 with 2.0 M ^{i}PrOH (or 100 mM phenol). The counter compartment consisted of 250 mM $^nBu_4NPF_6$ and 2.0 M NEt_3 with 2.0 M ^{i}PrOH (or 100 mM phenol). The working electrode was the oxidized Si

electrode **3**@SiO_x-porSi, **4**@SiO_x-porSi, or SiO_x-porSi$^{\Delta}$. The counter electrode was a graphite rod. The reference electrode was an Ag wire. Both compartments were sparged with CO_2 (with 5% of methane as GC internal standard) for 20 minutes before electrolysis, while stirring the working compartment. The cell was then sealed before CPE began. During the experiment, the solution in the working compartment was stirred at a speed of 1200 rpm. A VeraSol-2 LED solar simulator was used to illuminate the samples and the headspace was regularly sampled using a Shimadzu Nexis GC-2030 equipped with a thermal conductivity detector (TCD) for quantifying O_2, N_2, and H_2 gases, connected in series with a mechanizer and flame ionization detector (FID) for quantifying CO. Formate product was quantified using ion chromatography (IC) by taking 500 μL aliquots of the working solution. A 32-fold dilution of these aliquots using distilled water was performed followed by filtration through a 0.22 μm syringe filter prior to IC analysis using the same instrument described previously.

Supplemental Information

Supplemental information can be found online.

Acknowledgements

This work was solely supported as part of the Center for Hybrid Approaches in Solar Energy to Liquid Fuels (CHASE), an Energy Innovation Hub funded by the U.S. Department of Energy, Office of Science, Office of Basic Energy Sciences under Award Number DE-SC0021173. NH thanks the Yale Center for Natural Carbon Capture for support. HSN acknowledges support through a National Science Foundation Graduate Fellowship (2021315253). The IR instrument used in this study was purchased in 2018 with funds from the U.S. National Institutes of Health (R01GM50422), from the Air Force Office of Scientific Research under award number FA9550-18-1-0420 to a Multidisciplinary Research Program of the University Research Initiative (MURI) "Molecular-Scale Studies of Liquid−Solid Interfaces in Electrochemical Processes", and from the Center for Molecular Electrocatalysis (CME), an Energy Frontier Research Center funded by the U.S. Department of Energy, Office of Science, Office of Basic Energy Sciences. This work made use of instrumentation (XPS) at the Chapel Hill Analytical and Nanofabrication Laboratory, CHANL, a member of the North Carolina Research Triangle Nanotechnology Network, RTNN, which is supported by the National Science Foundation, Grant ECCS-2025064, as part of the National Nanotechnology Coordinated Infrastructure, NNCI. The STEM analysis was carried out

at the Singh Center for Nanotechnology, which is supported by the NSF National Nanotechnology Coordinated Infrastructure Program under grant NNCI-2025608 and the Laboratory for Research on the Structure of Matter (MRSEC) supported by the National Science Foundation (DMR-2309043). This work made use of equipment in the Chemical and Biophysical Instrumentation Center and Analytical and Stable Isotope Center at Yale University.

Author Contributions

YHH, XJ, JCW, JLA, AG, AK, BQM, and NP synthesized and characterized molecular complexes and performed catalytic experiments in solution. YHH, XJ, ESJ, JLA, CLD, MH, AK, HSN, and CQ prepared and characterized SiO_x-porSi wafers. YHH, XJ, ESJ, and AK immobilized the molecular catalysts and YHH, XJ, ESJ, CLD, SJ, JK, HK, YZ characterized the immobilized systems. YHH, XJ, and AK performed photoelectrocatalytic experiments using immobilized complexes. ESJ and NJG performed OCP measurements. YHH, XJ, and ESJ wrote the first draft of the manuscript, and all authors revised the text. NH, JMM, and ES supervised the research and obtained funding.

Declaration of Interests

Several authors of this work have a PCT Application on the use of porous Si and oxidized porous Si as a support for molecular catalysts.

References

1. Quadrelli, E. A.; Centi, G.; Duplan, J.-L.; Perathoner, S. Carbon Dioxide Recycling: Emerging Large-Scale Technologies with Industrial Potential. *ChemSusChem* **2011**, *4*, 1194, https://doi.org/10.1002/cssc.201100473.
2. Schneider, J.; Jia, H.; Muckerman, J. T.; Fujita, E. Thermodynamics and Kinetics of CO_2, CO, and H^+ Binding to the Metal Centre of CO_2 Reduction Catalysts. *Chem. Soc. Rev.* **2012**, *41*, 2036, https://doi.org/10.1039/C1CS15278E.
3. Appel, A. M.; Bercaw, J. E.; Bocarsly, A. B.; Dobbek, H.; DuBois, D. L.; Dupuis, M.; Ferry, J. G.; Fujita, E.; Hille, R.; Kenis, P. J. A.; Kerfeld, C. A.; Morris, R. H.; Peden, C. H. F.; Portis, A. R.; Ragsdale, S. W.; Rauchfuss, T. B.; Reek, J. N. H.; Seefeldt, L. C.; Thauer, R. K.; Waldrop, G. L. Frontiers, Opportunities, and Challenges in Biochemical and Chemical Catalysis of CO_2 Fixation. *Chem. Rev.* **2013**, *113*, 6621, https://doi.org/10.1021/cr300463y.
4. Wang, W.-H.; Himeda, Y.; Muckerman, J. T.; Manbeck, G. F.; Fujita, E. CO_2 Hydrogenation to Formate and Methanol as an Alternative to Photo- and Electrochemical CO_2 Reduction. *Chem. Rev.* **2015**, *115*, 12936, https://doi.org/10.1021/acs.chemrev.5b00197.
5. Limbach, M. In *Adv. Organomet. Chem.*; Pérez, P. J., Ed.; Academic Press: 2015; Vol. 63, p 175.
6. Artz, J.; Müller, T. E.; Thenert, K.; Kleinekorte, J.; Meys, R.; Sternberg, A.; Bardow, A.; Leitner, W. Sustainable Conversion of Carbon Dioxide: An Integrated Review of Catalysis and Life Cycle Assessment. *Chem. Rev.* **2018**, *118*, 434, https://doi.org/10.1021/acs.chemrev.7b00435.
7. Burkart, M. D.; Hazari, N.; Tway, C. L.; Zeitler, E. L. Opportunities and Challenges for Catalysis in Carbon Dioxide Utilization. *ACS Catal.* **2019**, *9*, 7937, https://doi.org/10.1021/acscatal.9b02113.
8. Hepburn, C.; Adlen, E.; Beddington, J.; Carter, E. A.; Fuss, S.; Mac Dowell, N.; Minx, J. C.; Smith, P.; Williams, C. K. The Technological and Economic Prospects for CO_2 Utilization and Removal. *Nature* **2019**, *575*, 87, https://doi.org/10.1038/s41586-019-1681-6.
9. Zhang, Z.; Pan, S.-Y.; Li, H.; Cai, J.; Olabi, A. G.; Anthony, E. J.; Manovic, V. Recent Advances in Carbon Dioxide Utilization. *Renew. Sustain. Energy Rev.* **2020**, *125*, 109799, https://doi.org/10.1016/j.rser.2020.109799.

10. Gao, W.; Liang, S.; Wang, R.; Jiang, Q.; Zhang, Y.; Zheng, Q.; Xie, B.; Toe, C. Y.; Zhu, X.; Wang, J.; Huang, L.; Gao, Y.; Wang, Z.; Jo, C.; Wang, Q.; Wang, L.; Liu, Y.; Louis, B.; Scott, J.; Roger, A.-C.; Amal, R.; He, H.; Park, S.-E. Industrial Carbon Dioxide Capture and Utilization: State of the Art and Future Challenges. *Chem. Soc. Rev.* **2020**, *49*, 8584, https://doi.org/10.1039/D0CS00025F.
11. Grice, K. A. Carbon Dioxide Reduction with Homogenous Early Transition Metal Complexes: Opportunities and Challenges for Developing CO_2 Catalysis. *Coord. Chem. Rev.* **2017**, *336*, 78, https://doi.org/10.1016/j.ccr.2017.01.007.
12. Tappe, N. A.; Reich, R. M.; D'Elia, V.; Kühn, F. E. Current Advances in the Catalytic Conversion of Carbon Dioxide by Molecular Catalysts: An Update. *Dalton Trans.* **2018**, *47*, 13281, https://doi.org/10.1039/C8DT02346H.
13. Yeung, C. S. Photoredox Catalysis as a Strategy for CO_2 Incorporation: Direct Access to Carboxylic Acids from a Renewable Feedstock. *Angew. Chem. Int. Ed.* **2019**, *58*, 5492, https://doi.org/10.1002/anie.201806285.
14. Nandal, N.; Jain, S. L. A Review on Progress and Perspective of Molecular Catalysis in Photoelectrochemical Reduction of CO_2. *Coord. Chem. Rev.* **2022**, *451*, 214271, https://doi.org/10.1016/j.ccr.2021.214271.
15. Fujita, E.; Grills, D. C.; Manbeck, G. F.; Polyansky, D. E. Understanding the Role of Inter- and Intramolecular Promoters in Electro- and Photochemical CO_2 Reduction Using Mn, Re, and Ru Catalysts. *Acc. Chem. Res.* **2022**, *55*, 616, https://doi.org/10.1021/acs.accounts.1c00616.
16. Qiao, J.; Liu, Y.; Hong, F.; Zhang, J. A Review of Catalysts for the Electroreduction of Carbon Dioxide to Produce Low-Carbon Fuels. *Chem. Soc. Rev.* **2014**, *43*, 631, https://doi.org/10.1039/C3CS60323G.
17. Zheng, T.; Jiang, K.; Wang, H. Recent Advances in Electrochemical CO_2-to-CO Conversion on Heterogeneous Catalysts. *Adv. Mater.* **2018**, *30*, 1802066, https://doi.org/10.1002/adma.201802066.
18. Xu, S.; Carter, E. A. Theoretical Insights into Heterogeneous (Photo)electrochemical CO_2 Reduction. *Chem. Rev.* **2019**, *119*, 6631, https://doi.org/10.1021/acs.chemrev.8b00481.
19. Sun, L.; Reddu, V.; Fisher, A. C.; Wang, X. Electrocatalytic Reduction of Carbon Dioxide: Opportunities with Heterogeneous Molecular Catalysts. *Energy Environ. Sci.* **2020**, *13*, 374, https://doi.org/10.1039/C9EE03660A.
20. Creissen, C. E.; Fontecave, M. Solar-Driven Electrochemical CO_2 Reduction with Heterogeneous Catalysts. *Adv. Energ. Mater.* **2021**, *11*, 2002652, https://doi.org/10.1002/aenm.202002652.
21. Ma, Y.; Wang, J.; Yu, J.; Zhou, J.; Zhou, X.; Li, H.; He, Z.; Long, H.; Wang, Y.; Lu, P.; Yin, J.; Sun, H.; Zhang, Z.; Fan, Z. Surface Modification of Metal Materials for High-Performance Electrocatalytic Carbon Dioxide Reduction. *Matter* **2021**, *4*, 888, https://doi.org/10.1016/j.matt.2021.01.007.
22. Yoshino, S.; Takayama, T.; Yamaguchi, Y.; Iwase, A.; Kudo, A. CO_2 Reduction Using Water as an Electron Donor over Heterogeneous Photocatalysts Aiming at Artificial Photosynthesis. *Acc. Chem. Res.* **2022**, *55*, 966, https://doi.org/10.1021/acs.accounts.1c00676.
23. Serna, P.; Gates, B. C. Molecular Metal Catalysts on Supports: Organometallic Chemistry Meets Surface Science. *Acc. Chem. Res.* **2014**, *47*, 2612, https://doi.org/10.1021/ar500170k.
24. Copéret, C.; Comas-Vives, A.; Conley, M. P.; Estes, D. P.; Fedorov, A.; Mougel, V.; Nagae, H.; Núñez-Zarur, F.; Zhizhko, P. A. Surface Organometallic and Coordination Chemistry toward Single-Site Heterogeneous Catalysts: Strategies, Methods, Structures, and Activities. *Chem. Rev.* **2016**, *116*, 323, https://doi.org/10.1021/acs.chemrev.5b00373.
25. Hübner, S.; de Vries, J. G.; Farina, V. Why Does Industry Not Use Immobilized Transition Metal Complexes as Catalysts? *Adv. Synth. Catal.* **2016**, *358*, 3, https://doi.org/10.1002/adsc.201500846.
26. Witzke, R. J.; Chapovetsky, A.; Conley, M. P.; Kaphan, D. M.; Delferro, M. Nontraditional Catalyst Supports in Surface Organometallic Chemistry. *ACS Catal.* **2020**, *10*, 11822, https://doi.org/10.1021/acscatal.0c03350.
27. Bullock, R. M.; Das, A. K.; Appel, A. M. Surface Immobilization of Molecular Electrocatalysts for Energy Conversion. *Chem. Eur. J.* **2017**, *23*, 7626, https://doi.org/10.1002/chem.201605066.
28. Dalle, K. E.; Warnan, J.; Leung, J. J.; Reuillard, B.; Karmel, I. S.; Reisner, E. Electro- and Solar-Driven Fuel Synthesis with First Row Transition Metal Complexes. *Chem. Rev.* **2019**, *119*, 2752, https://doi.org/10.1021/acs.chemrev.8b00392.
29. Corbin, N.; Zeng, J.; Williams, K.; Manthiram, K. Heterogeneous Molecular Catalysts for Electrocatalytic CO_2 Reduction. *Nano Res.* **2019**, *12*, 2093, https://doi.org/10.1007/s12274-019-2403-y.
30. Liu, H.-Y.; Cody, C. C.; Jacob-Dolan, J. A.; Crabtree, R. H.; Brudvig, G. W. Surface-Attached Molecular Catalysts on Visible-Light-Absorbing Semiconductors: Opportunities and Challenges for a Stable Hybrid Water-Splitting Photoanode. *ACS Energy Lett.* **2020**, *5*, 3195, https://doi.org/10.1021/acsenergylett.0c01719.
31. Zhang, S.; Fan, Q.; Xia, R.; Meyer, T. J. CO_2 Reduction: From Homogeneous to Heterogeneous Electrocatalysis. *Acc. Chem. Res.* **2020**, *53*, 255, https://doi.org/10.1021/acs.accounts.9b00496.
32. Wu, Y.; Liang, Y.; Wang, H. Heterogeneous Molecular Catalysts of Metal Phthalocyanines for Electrochemical CO_2 Reduction Reactions. *Acc. Chem. Res.* **2021**, *54*, 3149, https://doi.org/10.1021/acs.accounts.1c00200.

33. Morikawa, T.; Sato, S.; Sekizawa, K.; Suzuki, T. M.; Arai, T. Solar-Driven CO_2 Reduction Using a Semiconductor/Molecule Hybrid Photosystem: From Photocatalysts to a Monolithic Artificial Leaf. *Acc. Chem. Res.* **2022**, *55*, 933, https://doi.org/10.1021/acs.accounts.1c00564.
34. Rosser, T. E.; Windle, C. D.; Reisner, E. Electrocatalytic and Solar-Driven CO_2 Reduction to CO with a Molecular Manganese Catalyst Immobilized on Mesoporous TiO_2. *Angew. Chem. Int. Ed.* **2016**, *55*, 7388, https://doi.org/10.1002/anie.201601038.
35. Maurin, A.; Robert, M. Noncovalent Immobilization of a Molecular Iron-Based Electrocatalyst on Carbon Electrodes for Selective, Efficient CO_2-to-CO Conversion in Water. *J. Am. Chem. Soc.* **2016**, *138*, 2492, https://doi.org/10.1021/jacs.5b12652.
36. Zhang, X.; Wu, Z.; Zhang, X.; Li, L.; Li, Y.; Xu, H.; Li, X.; Yu, X.; Zhang, Z.; Liang, Y.; Wang, H. Highly Selective and Active CO_2 Reduction Electrocatalysts Based on Cobalt Phthalocyanine/Carbon Nanotube Hybrid Structures. *Nat. Commun.* **2017**, *8*, 14675, https://doi.org/10.1038/ncomms14675.
37. Hu, X.-M.; Rønne, M. H.; Pedersen, S. U.; Skrydstrup, T.; Daasbjerg, K. Enhanced Catalytic Activity of Cobalt Porphyrin in CO_2 Electroreduction upon Immobilization on Carbon Materials. *Angew. Chem. Int. Ed.* **2017**, *56*, 6468, https://doi.org/10.1002/anie.201701104.
38. Sato, S.; Saita, K.; Sekizawa, K.; Maeda, S.; Morikawa, T. Low-Energy Electrocatalytic CO_2 Reduction in Water over Mn-Complex Catalyst Electrode Aided by a Nanocarbon Support and K^+ Cations. *ACS Catal.* **2018**, *8*, 4452, https://doi.org/10.1021/acscatal.8b01068.
39. Abdinejad, M.; Dao, C.; Deng, B.; Sweeney, M. E.; Dielmann, F.; Zhang, X.-a.; Kraatz, H. B. Enhanced Electrochemical Reduction of CO_2 to CO upon Immobilization onto Carbon Nanotubes Using an Iron-Porphyrin Dimer. *ChemistrySelect* **2020**, *5*, 979, https://doi.org/10.1002/slct.201904580.
40. Shang, B.; Zhao, F.; Choi, C.; Jia, X.; Pauly, M.; Wu, Y.; Tao, Z.; Zhong, Y.; Harmon, N.; Maggard, P. A.; Lian, T.; Hazari, N.; Wang, H. Monolayer Molecular Functionalization Enabled by Acid-Base Interaction for High-Performance Photochemical CO_2 Reduction. *ACS Energy Lett.* **2022**, *7*, 2265, https://doi.org/10.1021/acsenergylett.2c01147.
41. Zhanaidarova, A.; Jones, S. C.; Despagnet-Ayoub, E.; Pimentel, B. R.; Kubiak, C. P. Re(tBu-bpy)$(CO)_3$Cl Supported on Multi-Walled Carbon Nanotubes Selectively Reduces CO_2 in Water. *J. Am. Chem. Soc.* **2019**, *141*, 17270, https://doi.org/10.1021/jacs.9b08445.
42. Zhang, X.; Wang, Y.; Gu, M.; Wang, M.; Zhang, Z.; Pan, W.; Jiang, Z.; Zheng, H.; Lucero, M.; Wang, H. Molecular Engineering of Dispersed Nickel Phthalocyanines on Carbon Nanotubes for Selective CO_2 Reduction. *Nat. Energ.* **2020**, *5*, 684, https://doi.org/10.1038/s41560-020-0667-9.
43. Jia, X.; Stewart-Jones, E.; Alvarez-Hernandez, J. L.; Bein, G. P.; Dempsey, J. L.; Donley, C. L.; Hazari, N.; Houck, M. N.; Li, M.; Mayer, J. M.; Nedzbala, H. S.; Powers, R. E. Photoelectrochemical CO_2 Reduction to CO Enabled by a Molecular Catalyst Attached to High-Surface-Area Porous Silicon. *J. Am. Chem. Soc.* **2024**, *146*, 7998, https://doi.org/10.1021/jacs.3c10837.
44. Parkinson, B. A.; Weaver, P. F. Photoelectrochemical Pumping of Enzymatic CO_2 Reduction. *Nature* **1984**, *309*, 148, https://doi.org/10.1038/309148a0.
45. Arai, T.; Sato, S.; Uemura, K.; Morikawa, T.; Kajino, T.; Motohiro, T. Photoelectrochemical Reduction of CO_2 in Water Under Visible-Light Irradiation by a p-Type InP Photocathode Modified with an Electropolymerized Ruthenium Complex. *Chem. Commun.* **2010**, *46*, 6944, https://doi.org/10.1039/C0CC02061C.
46. Arai, T.; Tajima, S.; Sato, S.; Uemura, K.; Morikawa, T.; Kajino, T. Selective CO_2 Conversion to Formate in Water Using a CZTS Photocathode Modified with a Ruthenium Complex Polymer. *Chem. Commun.* **2011**, *47*, 12664, https://doi.org/10.1039/C1CC16160A.
47. Sato, S.; Arai, T.; Morikawa, T.; Uemura, K.; Suzuki, T. M.; Tanaka, H.; Kajino, T. Selective CO_2 Conversion to Formate Conjugated with H_2O Oxidation Utilizing Semiconductor/Complex Hybrid Photocatalysts. *J. Am. Chem. Soc.* **2011**, *133*, 15240, https://doi.org/10.1021/ja204881d.
48. Kang, P.; Zhang, S.; Meyer, T. J.; Brookhart, M. Rapid Selective Electrocatalytic Reduction of Carbon Dioxide to Formate by an Iridium Pincer Catalyst Immobilized on Carbon Nanotube Electrodes. *Angew. Chem. Int. Ed.* **2014**, *53*, 8709, https://doi.org/10.1002/anie.201310722.
49. Huang, X.; Shen, Q.; Liu, J.; Yang, N.; Zhao, G. A CO_2 Adsorption-Enhanced Semiconductor/Metal-Complex Hybrid Photoelectrocatalytic Interface for Efficient Formate Production. *Energy Environ. Sci.* **2016**, *9*, 3161, https://doi.org/10.1039/C6EE00968A.
50. Kuriki, R.; Yamamoto, M.; Higuchi, K.; Yamamoto, Y.; Akatsuka, M.; Lu, D.; Yagi, S.; Yoshida, T.; Ishitani, O.; Maeda, K. Robust Binding between Carbon Nitride Nanosheets and a Binuclear Ruthenium(II) Complex Enabling Durable, Selective CO_2 Reduction under Visible Light in Aqueous Solution. *Angew. Chem. Int. Ed.* **2017**, *56*, 4867, https://doi.org/10.1002/anie.201701627.

51. Sekizawa, K.; Sato, S.; Arai, T.; Morikawa, T. Solar-Driven Photocatalytic CO-$_2$ Reduction in Water Utilizing a Ruthenium Complex Catalyst on p-Type Fe_2O_3 with a Multiheterojunction. *ACS Catal.* **2018**, *8*, 1405, https://doi.org/10.1021/acscatal.7b03244.
52. Liu, J.; Guo, C.; Hu, X.; Zhao, G. Bio-Proton Coupled Semiconductor/Metal-Complex Hybrid Photoelectrocatalytic Interface for Efficient CO_2 Reduction. *Green Chem.* **2019**, *21*, 339, https://doi.org/10.1039/C8GC03066A.
53. Toyodome, T.; Amao, Y.; Higashi, M. Photoelectrochemical Reduction of CO_2 to Formate over a Hybrid System of $CuInS_2$ Photocathode and Formate Dehydrogenase Under Visible-Light Irradiation. *New J. Chem.* **2021**, *45*, 14803, https://doi.org/10.1039/D1NJ02481G.
54. Nandal, N.; Manwar, N. R.; Abraham, B. M.; Khatri, P. K.; Jain, S. L. Photoelectrochemical Reduction of CO_2 Promoted by a Molecular Hybrid Made Up of Co(II)Pc on Graphene Oxide under Visible Light Illumination. *Energy Fuels* **2022**, *36*, 3760, https://doi.org/10.1021/acs.energyfuels.2c00096.
55. Bulushev, D. A.; Ross, J. R. H. Towards Sustainable Production of Formic Acid. *ChemSusChem* **2018**, *11*, 821, https://doi.org/10.1002/cssc.201702075.
56. Rice, C.; Ha, S.; Masel, R. I.; Waszczuk, P.; Wieckowski, A.; Barnard, T. Direct Formic Acid Fuel Cells. *J. Power Sources* **2002**, *111*, 83, https://doi.org/10.1016/S0378-7753(02)00271-9.
57. Johnson, T. C.; Morris, D. J.; Wills, M. Hydrogen Generation from Formic Acid and Alcohols Using Homogeneous Catalysts. *Chem. Soc. Rev.* **2010**, *39*, 81, https://doi.org/10.1039/B904495G.
58. Mellmann, D.; Sponholz, P.; Junge, H.; Beller, M. Formic Acid as a Hydrogen Storage Material-Development of Homogeneous Catalysts for Selective Hydrogen Release. *Chem. Soc. Rev.* **2016**, *45*, 3954, https://doi.org/10.1039/C5CS00618J.
59. Siffert, P.; Krimmel, E. *Silicon: Evolution and Future of a Technology*; Springer Science: New York, 2013.
60. Huang, K.; Duclairoir, F.; Pro, T.; Buckley, J.; Marchand, G.; Martinez, E.; Marchon, J.-C.; De Salvo, B.; Delapierre, G.; Vinet, F. Ferrocene and Porphyrin Monolayers on Si(100) Surfaces: Preparation and Effect of Linker Length on Electron Transfer. *ChemPhysChem* **2009**, *10*, 963, https://doi.org/10.1002/cphc.200800818.
61. Fabre, B. Ferrocene-Terminated Monolayers Covalently Bound to Hydrogen-Terminated Silicon Surfaces. Toward the Development of Charge Storage and Communication Devices. *Acc. Chem. Res.* **2010**, *43*, 1509, https://doi.org/10.1021/ar100085q.
62. Moore, G. F.; Sharp, I. D. A Noble-Metal-Free Hydrogen Evolution Catalyst Grafted to Visible Light-Absorbing Semiconductors. *J. Phys. Chem. Lett.* **2013**, *4*, 568, https://doi.org/10.1021/jz400028z.
63. Seo, J.; Pekarek, R. T.; Rose, M. J. Photoelectrochemical Operation of a Surface-Bound, Nickel-Phosphine H_2 Evolution Catalyst on p-Si(111): A Molecular Semiconductor|Catalyst Construct. *Chem. Commun.* **2015**, *51*, 13264, https://doi.org/10.1039/C5CC02802G.
64. Gurrentz, J. M.; Rose, M. J. Non-Catalytic Benefits of Ni(II) Binding to an Si(111)-PNP Construct for Photoelectrochemical Hydrogen Evolution Reaction: Metal Ion Induced Flat Band Potential Modulation. *J. Am. Chem. Soc.* **2020**, *142*, 5657, https://doi.org/10.1021/jacs.9b12824.
65. Reyes Cruz, E. A.; Nishiori, D.; Wadsworth, B. L.; Nguyen, N. P.; Hensleigh, L. K.; Khusnutdinova, D.; Beiler, A. M.; Moore, G. F. Molecular-Modified Photocathodes for Applications in Artificial Photosynthesis and Solar-to-Fuel Technologies. *Chem. Rev.* **2022**, *122*, 16051, https://doi.org/10.1021/acs.chemrev.2c00200.
66. Jia, X.; Nedzbala, H. S.; Bottum, S. R.; Cahoon, J. F.; Concepcion, J. J.; Donley, C. L.; Gang, A.; Han, Q.; Hazari, N.; Kessinger, M. C.; Lockett, M. R.; Mayer, J. M.; Mercado, B. Q.; Meyer, G. J.; Pearce, A. J.; Rooney, C. L.; Sampaio, R. N.; Shang, B.; Wang, H. Synthesis and Surface Attachment of Molecular Re(I) Complexes Supported by Functionalized Bipyridyl Ligands. *Inorg. Chem.* **2023**, *62*, 2359, https://doi.org/10.1021/acs.inorgchem.2c04137.
67. Morita, M.; Ohmi, T.; Hasegawa, E.; Kawakami, M.; Ohwada, M. Growth of Native Oxide on a Silicon Surface. *J. Appl. Phys.* **1990**, *68*, 1272, https://doi.org/10.1063/1.347181.
68. Niwano, M.; Kageyama, J. i.; Kurita, K.; Kinashi, K.; Takahashi, I.; Miyamoto, N. Infrared Spectroscopy Study of Initial Stages of Oxidation of Hydrogen-Terminated Si Surfaces Stored in Air. *J. Appl. Phys.* **1994**, *76*, 2157, https://doi.org/10.1063/1.357627.
69. Herino, R.; Bomchil, G.; Barla, K.; Bertrand, C.; Ginoux, J. L. Porosity and Pore Size Distributions of Porous Silicon Layers. *J. Electrochem. Soc.* **1987**, *134*, 1994, https://doi.org/10.1149/1.2100805.
70. Northen, T. R.; Woo, H.-K.; Northen, M. T.; Nordström, A.; Uritboonthail, W.; Turner, K. L.; Siuzdak, G. High Surface Area of Porous Silicon Drives Desorption of Intact Molecules. *J. Am. Soc. Mass. Spectrom.* **2007**, *18*, 1945, https://doi.org/10.1016/j.jasms.2007.08.009.
71. Riikonen, J.; Salomäki, M.; van Wonderen, J.; Kemell, M.; Xu, W.; Korhonen, O.; Ritala, M.; MacMillan, F.; Salonen, J.; Lehto, V.-P. Surface Chemistry, Reactivity, and Pore Structure of Porous Silicon Oxidized by Various Methods. *Langmuir* **2012**, *28*, 10573, https://doi.org/10.1021/la301642w.

72. Schmeltzer, J. M.; Porter, L. A.; Stewart, M. P.; Buriak, J. M. Hydride Abstraction Initiated Hydrosilylation of Terminal Alkenes and Alkynes on Porous Silicon. *Langmuir* **2002**, *18*, 2971, https://doi.org/10.1021/la0156560.
73. For an example of room temperature hydrosilylation see reference 72 and the following article. However, these systems require additives to promote the hydrosilylation reaction that are not compatible with H-porSi: Purkait, T. K.; Iqbal, M.; Wahl, M. H.; Gottschling, K.; Gonzalez, C. M.; Islam, M. A.; Veinot, J. G. C. Borane-Catalyzed Room-Temperature Hydrosilylation of Alkenes/Alkynes on Silicon Nanocrystal Surfaces. *J. Am. Chem. Soc.* **2014**, *136*, 17914, https://doi.org/10.1021/ja510120e.
74. Glass, J. A.; Wovchko, E. A.; Yates, J. T. Reaction of Methanol with Porous Silicon. *Surf. Sci.* **1995**, *338*, 125, https://doi.org/10.1016/0039-6028(95)00599-4.
75. Sun, W.; Qian, C.; He, L.; Ghuman, K. K.; Wong, A. P. Y.; Jia, J.; Ali, F. M.; O'Brien, P. G.; Reyes, L. M.; Wood, T. E.; Helmy, A. S.; Mims, C. A.; Singh, C. V.; Ozin, G. A. Heterogeneous Reduction of Carbon Dioxide by Hydride-Terminated Silicon Nanocrystals. *Nat. Commun.* **2016**, *7*, 12553, https://doi.org/10.1038/ncomms12553.
76. Qian, C.; Sun, W.; Hung, D. L. H.; Qiu, C.; Makaremi, M.; Hari Kumar, S. G.; Wan, L.; Ghoussoub, M.; Wood, T. E.; Xia, M.; Tountas, A. A.; Li, Y. F.; Wang, L.; Dong, Y.; Gourevich, I.; Singh, C. V.; Ozin, G. A. Catalytic CO_2 Reduction by Palladium-Decorated Silicon-Hydride Nanosheets. *Nat. Catal.* **2019**, *2*, 46, https://doi.org/10.1038/s41929-018-0199-x.
77. Sun, K.; Shen, S.; Liang, Y.; Burrows, P. E.; Mao, S. S.; Wang, D. Enabling Silicon for Solar-Fuel Production. *Chem. Rev.* **2014**, *114*, 8662, https://doi.org/10.1021/cr300459q.
78. Pujari, S. P.; Scheres, L.; Marcelis, A. T. M.; Zuilhof, H. Covalent Surface Modification of Oxide Surfaces. *Angew. Chem. Int. Ed.* **2014**, *53*, 6322, https://doi.org/10.1002/anie.201306709.
79. Kim, D.; Zuidema, J. M.; Kang, J.; Pan, Y.; Wu, L.; Warther, D.; Arkles, B.; Sailor, M. J. Facile Surface Modification of Hydroxylated Silicon Nanostructures Using Heterocyclic Silanes. *J. Am. Chem. Soc.* **2016**, *138*, 15106, https://doi.org/10.1021/jacs.6b08614.
80. A Mini Review: Recent Advances in Surface Modification of Porous Silicon.
81. Wallart, X.; Henry de Villeneuve, C.; Allongue, P. Truly Quantitative XPS Characterization of Organic Monolayers on Silicon: Study of Alkyl and Alkoxy Monolayers on H-Si(111). *J. Am. Chem. Soc.* **2005**, *127*, 7871, https://doi.org/10.1021/ja0430797.
82. Huck, L. A.; Buriak, J. M. In *Handbook of Porous Silicon*; Canham, L. (Ed); Springer International Publishing, **2021**, Cham, Switzerland.
83. Chazalviel, J. N.; Ozanam, F. Surface Chemistry of Porous Silicon. *MRS Online Proceedings Library* **1998**, *536*, 155, https://doi.org/10.1557/PROC-536-155.
84. Labunov, V.; Bondarenko, V.; Glinenko, I.; Dorofeev, A.; Tabulina, L. Heat Treatment Effect on Porous Silicon. *Thin Solid Films* **1986**, *137*, 123, https://doi.org/10.1016/0040-6090(86)90200-2.
85. Pap, A.; Kordás, K.; Toth, G.; Levoska, J.; Uusimäki, A.; Vähäkangas, J.; Leppävuori, S.; George, T.; Sio, V.; Si, V.; Sio, S.; Sio; Si, M. Thermal Oxidation of Porous Silicon: Study on Structure. *Appl. Phys. Lett.* **2005**, *86*, 041501, https://doi.org/10.1063/1.1853519.
86. Mawhinney, D. B.; Glass, J. A.; Yates, J. T. FTIR Study of the Oxidation of Porous Silicon. *J. Phys. Chem. B* **1997**, *101*, 1202, https://doi.org/10.1021/jp963322r.
87. For this type of semiquantitative IR spectroscopy, it is important to sample the exact same area of the wafer. In our case, we always carefully center the sample and set the beam aperture to match most of the sample to ensure reproducibility in our measurements.
88. Murphy, J. D.; McGuire, R. E.; Bothe, K.; Voronkov, V. V.; Falster, R. J. Minority Carrier Lifetime in Silicon Photovoltaics: The Effect of Oxygen Precipitation. *Sol. Energy Mater. Sol. Cells* **2014**, *120*, 402, https://doi.org/10.1016/j.solmat.2013.06.018.
89. For a porous material, it is possible that electrons can penetrate deeper than 10 nm, but our pore depth is on the order of micrometers, so it is unlikely that electrons can penetrate fully into the pores.
90. Cerofolini, G. F.; Galati, C.; Renna, L. Si 2p XPS Spectrum of the Hydrogen-Terminated (100) Surface of Device-Quality Silicon. *Surf. Interface Anal.* **2003**, *35*, 968, https://doi.org/10.1002/sia.1632.
91. Aureau, D.; Bouttemy, M.; Vigneron, J.; Chazalviel, J.-N.; Ozanam, F.; Etcheberry, A. XPS Analysis of Porous Silicon. *ECS Trans.* **2013**, *50*, 107, https://doi.org/10.1149/05037.0107ecst.
92. Madsen, M. R.; Rønne, M. H.; Heuschen, M.; Golo, D.; Ahlquist, M. S. G.; Skrydstrup, T.; Pedersen, S. U.; Daasbjerg, K. Promoting Selective Generation of Formic Acid from CO_2 Using $Mn(bpy)(CO)_3Br$ as Electrocatalyst and Triethylamine/Isopropanol as Additives. *J. Am. Chem. Soc.* **2021**, *143*, 20491, https://doi.org/10.1021/jacs.1c10805.
93. Frye, C. L.; Vincent, G. A.; Finzel, W. A. Pentacoordinate Silicon Compounds. V. Novel Silatrane Chemistry. *J. Am. Chem. Soc.* **1971**, *93*, 6805, https://doi.org/10.1021/ja00754a017.

94. Materna, K. L.; Brennan, B. J.; Brudvig, G. W. Silatranes for Binding Inorganic Complexes to Metal Oxide Surfaces. *Dalton Trans.* **2015**, *44*, 20312, https://doi.org/10.1039/C5DT03463A.
95. Materna, K. L.; Rudshteyn, B.; Brennan, B. J.; Kane, M. H.; Bloomfield, A. J.; Huang, D. L.; Shopov, D. Y.; Batista, V. S.; Crabtree, R. H.; Brudvig, G. W. Heterogenized Iridium Water-Oxidation Catalyst from a Silatrane Precursor. *ACS Catal.* **2016**, *6*, 5371, https://doi.org/10.1021/acscatal.6b01101.
96. Materna, K. L.; Jiang, J.; Crabtree, R. H.; Brudvig, G. W. Silatrane Anchors for Metal Oxide Surfaces: Optimization for Potential Photocatalytic and Electrocatalytic Applications. *ACS Appl. Mater. Interfaces.* **2019**, *11*, 5602, https://doi.org/10.1021/acsami.8b04138.
97. Troiano, J. L.; Crabtree, R. H.; Brudvig, G. W. Optimization of Surface Loading of the Silatrane Anchoring Group on TiO_2. *ACS Appl. Mater. Interfaces.* **2022**, *14*, 6582, https://doi.org/10.1021/acsami.1c20678.
98. Henry, L.; Schneider, C.; Mützel, B.; Simpson, P. V.; Nagel, C.; Fucke, K.; Schatzschneider, U. Amino Acid Bioconjugation via iClick Reaction of an Oxanorbornadiene-Masked Alkyne with a $Mn^{I}(bpy)(CO)_3$-Coordinated Azide. *Chem. Commun.* **2014**, *50*, 15692, https://doi.org/10.1039/C4CC07892F.
99. Pordel, S.; Schrage, B. R.; Ziegler, C. J.; White, J. K. Impact of Steric Bulk on Photoinduced Ligand Exchange Reactions in Mn(I) PhotoCORMs. *Inorg. Chim. Acta* **2020**, *511*, 119845, https://doi.org/10.1016/j.ica.2020.119845.
100. Bourrez, M.; Molton, F.; Chardon-Noblat, S.; Deronzier, A. [Mn(bipyridyl)$(CO)_3$Br]: An Abundant Metal Carbonyl Complex as Efficient Electrocatalyst for CO_2 Reduction. *Angew. Chem. Int. Ed.* **2011**, *50*, 9903, https://doi.org/10.1002/anie.201103616.
101. Smieja, J. M.; Sampson, M. D.; Grice, K. A.; Benson, E. E.; Froehlich, J. D.; Kubiak, C. P. Manganese as a Substitute for Rhenium in CO_2 Reduction Catalysts: The Importance of Acids. *Inorg. Chem.* **2013**, *52*, 2484, https://doi.org/10.1021/ic302391u.
102. Stanbury, M.; Compain, J.-D.; Chardon-Noblat, S. Electro and Photoreduction of CO_2 Driven by Manganese-Carbonyl Molecular Catalysts. *Coord. Chem. Rev.* **2018**, *361*, 120, https://doi.org/10.1016/j.ccr.2018.01.014.
103. Rønne, M. H.; Cho, D.; Madsen, M. R.; Jakobsen, J. B.; Eom, S.; Escoudé, É.; Hammershøj, H. C. D.; Nielsen, D. U.; Pedersen, S. U.; Baik, M.-H.; Skrydstrup, T.; Daasbjerg, K. Ligand-Controlled Product Selectivity in Electrochemical Carbon Dioxide Reduction Using Manganese Bipyridine Catalysts. *J. Am. Chem. Soc.* **2020**, *142*, 4265, https://doi.org/10.1021/jacs.9b11806.
104. Huffman, B. L.; Bein, G. P.; Atallah, H.; Donley, C. L.; Alameh, R. T.; Wheeler, J. P.; Durand, N.; Harvey, A. K.; Kessinger, M. C.; Chen, C. Y.; Fakhraai, Z.; Atkin, J. M.; Castellano, F. N.; Dempsey, J. L. Surface Immobilization of a Re(I) Tricarbonyl Phenanthroline Complex to Si(111) through Sonochemical Hydrosilylation. *ACS Appl. Mater. Interfaces* **2023**, *15*, 984, https://doi.org/10.1021/acsami.2c17078.
105. Biesinger, M. C.; Payne, B. P.; Grosvenor, A. P.; Lau, L. W. M.; Gerson, A. R.; Smart, R. S. C. Resolving Surface Chemical States in XPS Analysis of First Row Transition Metals, Oxides and Hydroxides: Cr, Mn, Fe, Co and Ni. *Appl. Surf. Sci.* **2011**, *257*, 2717, https://doi.org/10.1016/j.apsusc.2010.10.051.
106. Pennycook, S. J. and Nellist, P. D. (Eds). *Scanning Transmission Electron Microscopy: Imaging and Analysis*. Springer Science & Business Media, **2011**, New York.
107. Cosandey, F. Analysis of Li-Ion Battery Materials by Electron Energy Loss Spectroscopy. *Microscopy: Science, Technology, Applications, and Education* **2010**, 1662,
108. For this study, we define the onset potential as the point where there is a 0.1 mA/cm^2 difference in current density between the cyclic voltammograms for electrocatalysis under CO_2 versus that under similar conditions except under Ar.
109. The geometric current density reported in this study is calculated using the geometric area of the porous region of the wafer.
110. Beiler, A. M.; McCarthy, B. D.; Johnson, B. A.; Ott, S. Enhancing Photovoltages at p-type Semiconductors Through a Redox-Active Metal-Organic Framework Surface Coating. *Nat. Commun.* **2020**, *11*, 5819, https://doi.org/10.1038/s41467-020-19483-5.
111. Laurans, M.; Wells, J. A. L.; Ott, S. Immobilising Molecular Ru Complexes on a Protective Ultrathin Oxide Layer of p-Si Electrodes Towards Photoelectrochemical CO_2 Reduction. *Dalton Trans.* **2021**, *50*, 10482, https://doi.org/10.1039/D1DT01331A.
112. Jia, X.; Cui, K.; Alvarez-Hernandez, J. L.; Donley, C. L.; Gang, A.; Hammes-Schiffer, S.; Hazari, N.; Jeon, S.; Mayer, J. M.; Nedzbala, H. S.; Shang, B.; Stach, E. A.; Stewart-Jones, E.; Wang, H.; Williams, A. Synthesis and Surface Attachment of Molecular Re(I) Hydride Species with Silatrane Functionalized Bipyridyl Ligands. *Organometallics* **2023**, *42*, 2238, https://doi.org/10.1021/acs.organomet.3c00235.
113. Bein, G. P.; Stewart, M. A.; Assaf, E. A.; Tereniak, S. J.; Sampaio, R. N.; Miller, A. J. M.; Dempsey, J. L. Methyl Termination of p-Type Silicon Enables Selective Photoelectrochemical CO_2 Reduction by a Molecular Ruthenium Catalyst. *ACS Energy Lett.* **2024**, *9*, 1777, https://doi.org/10.1021/acsenergylett.4c00122.

114. Shang, B.; Rooney, C. L.; Gallagher, D. J.; Wang, B. T.; Krayev, A.; Shema, H.; Leitner, O.; Harmon, N. J.; Xiao, L.; Sheehan, C.; Bottum, S. R.; Gross, E.; Cahoon, J. F.; Mallouk, T. E.; Wang, H. Aqueous Photoelectrochemical CO_2 Reduction to CO and Methanol over a Silicon Photocathode Functionalized with a Cobalt Phthalocyanine Molecular Catalyst. *Angew. Chem. Int. Ed.* **2023**, *62*, e202215213, https://doi.org/10.1002/anie.202215213.
115. Wise, C. F.; Agarwal, R. G.; Mayer, J. M. Determining Proton-Coupled Standard Potentials and X–H Bond Dissociation Free Energies in Nonaqueous Solvents Using Open-Circuit Potential Measurements. *J. Am. Chem. Soc.* **2020**, *142*, 10681, https://doi.org/10.1021/jacs.0c01032.
116. Agarwal, R. G.; Coste, S. C.; Groff, B. D.; Heuer, A. M.; Noh, H.; Parada, G. A.; Wise, C. F.; Nichols, E. M.; Warren, J. J.; Mayer, J. M. Free Energies of Proton-Coupled Electron Transfer Reagents and Their Applications. *Chem. Rev.* **2022**, *122*, 1, https://doi.org/10.1021/acs.chemrev.1c00521.
117. Green, M. L.; Gusev, E. P.; Degraeve, R.; Garfunkel, E. L. Ultrathin (<4 nm) and Si-O-N Gate Dielectric Layers for Silicon Microelectronics: Understanding the Processing, Structure, and Physical and Electrical Limits. *J. Appl. Phys.* **2001**, *90*, 2057, https://doi.org/10.1063/1.1385803.
118. Weck, M.; Jones, C. W. Mizoroki−Heck Coupling Using Immobilized Molecular Precatalysts: Leaching Active Species from Pd Pincers, Entrapped Pd Salts, and Pd NHC Complexes. *Inorg. Chem.* **2007**, *46*, 1865, https://doi.org/10.1021/ic061898h.
119. Sampson, M. D.; Nguyen, A. D.; Grice, K. A.; Moore, C. E.; Rheingold, A. L.; Kubiak, C. P. Manganese Catalysts with Bulky Bipyridine Ligands for the Electrocatalytic Reduction of Carbon Dioxide: Eliminating Dimerization and Altering Catalysis. *J. Am. Chem. Soc.* **2014**, *136*, 5460, https://doi.org/10.1021/ja501252f.
120. Kuo, H.-Y.; Tignor, S. E.; Lee, T. S.; Ni, D.; Park, J. E.; Scholes, G. D.; Bocarsly, A. B. Reduction-Induced CO Dissociation by a $[Mn(bpy)(CO)_4][SbF_6]$ Complex and its Relevance in Electrocatalytic CO_2 Reduction. *Dalton Trans.* **2020**, *49*, 891, https://doi.org/10.1039/C9DT04150H.
121. Rønne, M. H.; Madsen, M. R.; Skrydstrup, T.; Pedersen, S. U.; Daasbjerg, K. Mechanistic Elucidation of Dimer Formation and Strategies for Its Suppression in Electrochemical Reduction of Fac-$Mn(bpy)(CO)_3Br$. *ChemElectroChem* **2021**, *8*, 2108, https://doi.org/10.1002/celc.202100279.

TOC Graphic

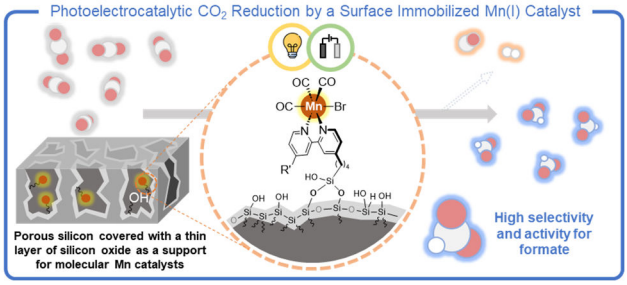
Photoelectrocatalytic CO_2 Reduction by a Surface Immobilized Mn(I) Catalyst
Porous silicon covered with a thin layer of silicon oxide as a support for molecular Mn catalysts
High selectivity and activity for formate